DTU Library

Multiscale characterisation of strains in semicrystalline polymers

Olsen, Ulrik L.; Laursen, Mads G.; Mazurek, Piotr S.; Kehres, Jan; Mikkelsen, Lars P.; Skov, Anne L.; Poulsen, Henning F.

Manuscript as pdf
Springer Nature 2021 LaTeX template
Click here to access/download;Attachment to Manuscript;PolymerStrain_JourPolRes.pdf

Click here to view linked References

Multiscale characterisation of strains in semicrystalline polymers

Ulrik L. Olsen[1*], Mads G. Laursen[1], Piotr S. Mazurek[2], Jan Kehres[1], Lars P. Mikkelsen[3], Anne L. Skov[2] and Henning F. Poulsen[1]

[1*]Department of Physics, Technical University of Denmark, Fysikvej 1, Kgs. Lyngby, 2800, Denmark.
[2]Department of Chemical Engineering, Technical University of Denmark, Søltofts Plads 288A , Kgs. Lyngby, 2800, Denmark.
[3]Department of Wind Energy, Technical University of Denmark, Frederiksborgvej 399, Roskilde, 4000, Denmark.

*Corresponding author(s). E-mail(s): ullu@dtu.dk;

Abstract

A nondestructive probe for mapping elastic strains within polymers would be an asset for materials engineering: for validation of mechanical models and for understanding damage nucleation. As a step towards this aim we demonstrate an X-ray wide angle diffraction methodology probing strain tensor components on mesoscopic length scales, in the range 3-50 Å. We demonstrate its use on a 50 % semi-crystalline polyethylene sample subjected to tensile straining up to 8.8 %. The mesoscopic strains derived for the crystalline phase scale linearly with the macroscopic strain, in contrast to the crystallised volume fraction and the texture evolution. In the crystalline phase, the material becomes softer and exhibit a larger degree of alignment with decreasing distance in direct space. The inherent strain sensitivity is 10^{-5}. The prospect of 3D mapping of local strain and stress tensors is discussed.

Keywords: X-ray imaging, X-ray diffraction, Polymers, Strain

1 Introduction

Elastic strain plays a crucial role in the structural organisation of crystalline specimens. Examples are the formation of nanodots in semiconductors, dislocation structures in plastically deformed metals and the phase morphology generated by solid-state phase transformations. In terms of engineering, control of the elastic strain is vital to increase product lifetime. X-ray and neutron diffraction methods [1, 2] allow determination of the elastic strain tensor non-destructively as a function of (x,y,z) position within the specimen. Furthermore, using synchrotron radiation and x-ray optics, the dimension of the X-ray beam can be varied from 10 nm to 1 mm [3–6]. This has led to the establishment of a number of methods for strain scanning on the engineering scale [2, 7] as well as on the scale of the (embedded) grains and sub-grains [8–10].

In Poulsen *et al.* [11] it was demonstrated that wide angle diffraction with hard x-rays can be used also for characterising bulk stress and strain fields in glasses. The strain accuracy is approximately 10^{-4}. This approach has been used extensively for studies of inorganic glasses [12]. In these studies it is typically found that the macroscopic response is less stiff than the atomic next-neighbour bonds because of structural rearrangements at the scale of 4-10 Å.

To our knowledge, characterisation of strain in amorphous polymers with diffraction methods has not been reported and even for semi-crystalline polymers results are precious few. Stress characterisation is therefore largely based on destructive techniques, or optical methods relying on changes in the refractive index with stress, both with limited applicability [13]. Several studies [14–17] establishes that a constant relationship $\epsilon_{local}/\epsilon_{macro}$ between the strain measured with SAXS and the externally applied strain exist in the pre-yield elastic strain domain. For PE at 25^oC specifically $\epsilon_{local}/\epsilon_{macro}$ is 0.5 even as the crystallinity changes although the ratio changes slightly with temperature and for other materials. But rather than a method for mapping local strain the investigations are investigating the influence of straining on the lamellae stacks and the spherulites in semicrystalline polymers to understand the structural behaviour. The relative scarcity of non-destructive bulk investigations is remarkable, as the impact of understanding strain and stress in polymers within materials science and engineering parallels that of crystalline materials. As examples, polymers are extensively used as adhesive joints and as matrix material in fibre reinforced composites, both with major applications in the aerospace, automotive and wind energy sector. Residual stresses developed during the manufacturing process will often have undesired impact on the mechanical performance [18, 19] such as reduction of fatigue lifetime, distortion of shape and lower ductility.

For thermoplasts we are aware of three X-ray diffraction based studies. Nishida *et al.* reported strain behaviour in fibre reinforced high density polyethylene (HDPE) using the sine-square-psi method on one diffraction peak [20]. Hughes *et al.*, also studied a single peak of HDPE but without an analysis of the texture evolution 2011 [21]. Schneider performed a study of injection

molded polypropylene at strains up to 800 % using both small angle and wide angle diffraction [22].

It is characteristic of these publications that analysis schemes for strain characterisation of classical crystalline materials were applied. However, in contrast to metals or ceramics we lack a microscopic understanding of the generation of strain in polymers, and even a definition. The energy absorbed during loading is primarily transformed into entropic terms, and in a tensile experiment the pair correlation function between atoms - which is what is measured by wide angle x-ray scattering (WAXS) - will therefore change much less with increasing elongation than is the case for hard materials, such as the crystals and inorganic glasses. Moreover, the strain is likely to vary with distance in the mesoscopic 3-50 Å range, leading to corresponding variation of the WAXS signal with distance in reciprocal space, $|\vec{Q}|$. In a semicrystalline polymer the process is further complicated by possible loadsharing with the amorphous phase, and by texture evolution. As a result the measurement of strain based on wide angle diffraction may not be linearly related to the external load, and will depend on which mesoscopic length scale one probes.

In this article we aim to make a comprehensive study of WAXS based strain analysis to a prototype thermoplast, of relevance for engineering: polyethylene (PE). We introduce the above mentioned methodology for characterising glasses [11, 23], and show it provides an excellent strain resolution. Using this we study simultaneously the strain and texture evolution during an *in situ* tensile experiment, as a function of mesoscopic length scale. We believe such data is a good starting point for deriving a micromechanical model of strain in thermoplasts. In this article, however, the focus is on elucidating if and how x-ray diffraction can be used by engineers for mapping the strain tensor in thermoplasts. From the strain tensor the stress tensor can be determined by means of Hooke's law assuming a linear elastic material response.

2 Experimental set-up

The *in-situ* experiment took place at beamline BL04B2 at the SPring-8 synchrotron facility. A schematic of the set-up is shown in Fig. 1. The energy of the incident radiation was 61.4 keV. The X-ray beam was monochromatised and focused in the horizontal plane by means of a Si 220 bent crystal monochromator. The samples were illuminated with a 3×3 mm^2 beam in transmission geometry. The acquisition time of the diffraction patterns was on average 120 s. The area detector used was a XRD1621XN ES CT-grade detector from Perkin-Elmer (now Varex Imaging) with 2048×2048 pixels and an active area of 409.6×409.6 mm^2. With the detector positioned 329.5 mm from the sample, the transmission set-up allowed the acquisition of data within a Q-range of 0.5 to 6.2 Å^{-1}. The detector was positioned asymmetrically relative to the direct beam such that the Q-range was extended in the upwards direction (in the direction $\eta = 0$, cf Fig. 1). The beam stop shadowed for a region of the image; we use a software mask to disregard the signal from this region.
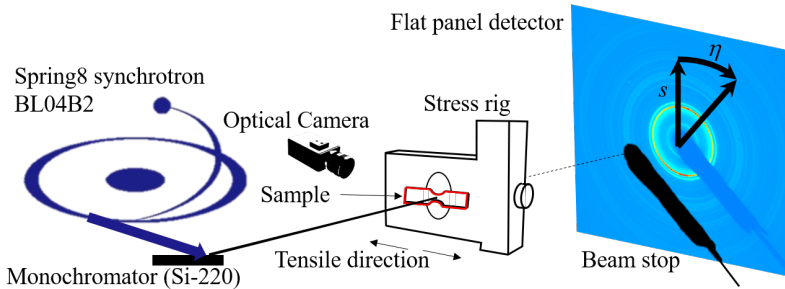
Fig. 1 Schematic diagram showing the high-energy X-ray diffraction setup used in the experiment. The sample was fixed in the stress rig at the side facing the detector, which is contrary to the schematic. An optical video sensor was mounted at an angle to capture optical images of the position of the sample during straining. The image on the 2D detector is an example of raw data with indication of zero points of the polar coordinates (s,η) used.

The material of choice was PE, acquired from Carlson & Möller, Helsingborg. The degree of crystallinity was determined using differential scanning calorimeter (DSC) Discovery from TA Instruments, USA. The specimens were exposed to heating/cooling at a rate of 10 °C min^{-1} in nitrogen atmosphere. The DSC measurement was repeated three times and results were averaged to give a final crystallinity of $50.1 \pm 0.5\%$.The density was determined using a pycnometer bottle and liquid immersion to be 0.922 g cm^{-3}. The sample was machined to a tensile test dog-bone with dimension 31mm×7mm×2.1mm (height, width, depth); the waist of the dogbone was machined as a round cutout 6.7 mm long and narrowing the test piece to 3.1 mm in the centre of the cutout making the smallest cross section area of the sample 6.5mm^2. The specimen geometry is also shown in Fig. 2.

Ionising radiation is known to influence the structure of polymers, giving rise to beam damage, see e.g. [24]. However, traditionally x-ray diffraction experiments are performed at much lower energies with a less favourable ratio between diffraction and absorption cross sections than in this experiment. In many cases the beam is furthermore poly-chromatic and originates from a small volume. The use of a high energy, monochromatic beam and a large sample volume at BL04B2 is assumed to make beam damage of the sample negligible. We performed a test of this assumption on a separate PE sample mounted in the same way as in the *in situ* experiment. Here diffraction patterns were continuously acquired during radiation for 2500 seconds. The acquisition time of each pattern was 1 second. The median of 12 exposures was used for each data point and including dead time each data point corresponds to 22 seconds of exposure.

For the tensile straining the dogbone sample was mounted in a Linkam TST350 thermomechanical tensile testing cell. The load stage was equipped with a 200 N load cell and self-centring grips which assured that the applied load was uniaxial. The load resolution of the cell was 10 mN, strain rates were 50 μm s^{-1} and strain resolution was specified to 1 μm.

During the experiment, the specimen was stretched in 11 steps of 40 μm, four steps of 120 μ m and two steps of 200μ m. Between each step the specimen was allowed to relax for $\approx$ 3 minutes; the stress values determined directly after each step has been used in the subsequent analysis. The drawing began from an unloaded state with a distance of 7.9 mm between stress rig grips and continued until an average elongation of 7.4% was achieved. At this point the specimen slipped in the grips. This final point is excluded from the data analysis, as well as the initial points until a positive stress on the sample was achieved.

Modelling the test-geometry using a 3-dimensional finite element model, a relation between the overall average strain, ϵ_a measured between the grips and the average strain, ϵ_{cent}, in the 3×3^{-2} mm central illuminated gauges section can be calculated. Taking an linear elastic isotropic material with $E = 203$ MPa and $\nu = 0.46$, a relation of $\epsilon_{cent} = 1.41\epsilon_a$ is found. In addition, the centre region will due to the constraining effect in the width direction in the notched region, have a lower apparent Poisons ratio given by $\nu_{cent} = 0.34\nu$.

Based on the average strain in the centre part of the test-geometry and the stresses calculated by the applied load divided by the narrow $3.1 \times$ 2.1 mm^2 cross-section, the recorded macroscopic stress-strain curve is reproduced in Fig. 2 with the strain steps indicated. A linear fit between 0% and 6.2% was used to determine macroscopic Young's modulus of 203 MPa in correspondence with the typical range of LDPE of 100-350 MPa [25].

3 Data analysis scheme

The data analysis follows the procedure established in Neuefeind *et al.* [23] - it is illustrated in Figs. 1 and 3. The nearly circular symmetric diffraction patterns are parameterised with respect to polar coordinates (s,η), see Fig. 1. In this work we divided the η-range of $[0 \ 2\pi]$ into 36 segments. Hence for $i = 1...36$ the i'th segment starts at $\eta_i = (i-1)*2\pi/36$. For each segment the intensity distribution

$$I'_i(Q) = \int_{\eta_i}^{\eta_i+\pi/18} I(Q,\eta)d\eta; \quad i = 1..36 \tag{1}$$

is determined, with $Q = Q(s)$ defined by Bragg's law. An example of such an intensity distribution $I'_i(Q)$ is shown in Fig. 3.

As a part of the conversion from raw data to 1D diffraction pattern the influence of the detector was corrected in terms of solid angle coverage and efficiency following the methodology in van Driel *et al.* [26]. The sample cross section decreases during strain according to the Poisson's ratio of the material leading to a decreasing diffraction interaction volume. In our analysis we assume that this effect decreases intensity isotropically and thus uniformly for all $I'_i(Q)$. This assumption is valid when the sample is much larger than
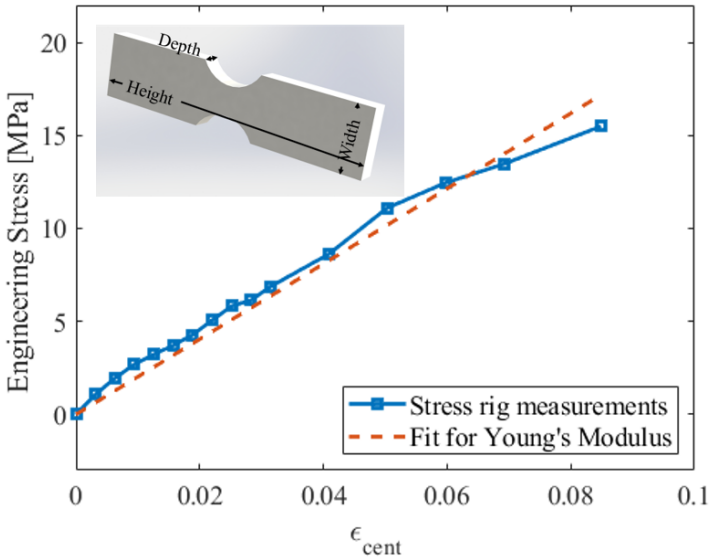
Fig. 2 The macroscopic stress-strain curve for the PE dogbone sample acquired during the experiment. The stress data is taken from the stress sensor directly as the strain step was reached disregarding any subsequent relaxation of stress before the next strain step. The strain was determined from the cumulative sum of steps taken from the operational interface since the strain from the images acquired with the optical camera had a considerably lower measurement precision. The insert shows the PE dogbone with dimensions indicated.

the beam in both directions perpendicular to the beam direction and when diffraction angles are small.

The diffraction pattern in Fig. 3 exhibits several distinct maxima, that we will associate with the "crystalline" phase. Following Bunn [27] and Nishida *et al.* [20] we identify the peaks (110), (200),(210) and (020) in Fig. 3 as belonging to an orthorhombic structure, with space group 62 (Pnma). From these data we find $a = 7.24$ Å and $b = 4.88$ Å. In comparison, Nishida *et al.* reported 7.4 Å and 4.9 Å for the same unit cell parameters for HDPE.

For each of these four main peaks of the "crystalline" phase and for each $I_i'(Q)$ the relative shift in position of the peak is determined with respect to the unloaded situation (subscript 0): $q_i = \frac{Q_i - Q_{i,0}}{Q_{i,0}}$. In the small strain limit q_i is the inverse of the corresponding strain in direct space $\epsilon_i = -q_i$. We have conservatively taken the threshold strain where this assumption holds to be 3%. To increase sensitivity, this analysis is performed by treating the unloaded distribution in the vicinity of the peak as a correlation function. The angular variation of the relative shifts ϵ_i thus obtained is fitted to the expression:

$$\epsilon_i = \epsilon_{11} \sin^2(\eta_i) + 2\epsilon_{12} \sin(\eta_i) \cos(\eta_i) + \epsilon_{22} \cos^2(\eta_i) \quad i = 1..36 \qquad (2)$$
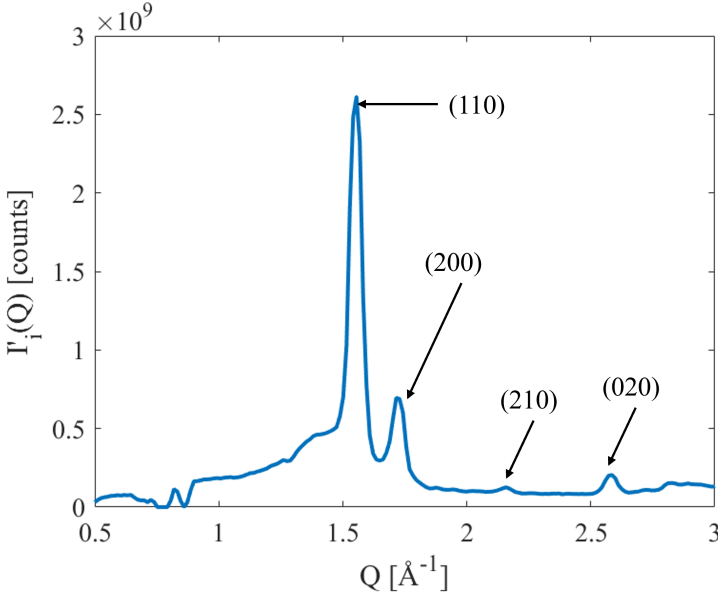
Fig. 3 Data analysis procedure. The raw data shown on the detector in Fig.1 are integrated azimuthally within 36 segments, an example of which ($\eta = 0$) is shown with the abscissa in units of Q. Four of the peaks belong to an orthorhombic phase - these are marked according to Miller indices.

As a result, three components of the strain tensor are determined: the axial (ϵ_{11}), tangential (ϵ_{22}) and in-plane shear component (ϵ_{12}). The expression comes from regular solid mechanics definition of the nine strain components [28]. The other strain components that are not in the plane perpendicular to the incoming beam can be determined from an experiment where the specimen is rotated around an axis perpendicular to the incoming beam.

To derive information on the mechanical properties we made a simple model of the diffraction intensity for PE as comprised of contributions from an "amorphous" phase and from the crystalline phase. As illustrated in Fig. 4 the crystalline part is represented by the four main peaks modelled as Gaussians. Following Monar *et al.* [29] in a crude approximation we model the amorphous phase by a Gaussian distribution. The model for the amorphous phase was fitted to the residual of the acquired pattern and the initial crystalline fit. The crystalline fit was then refined by fitting the model to the residual of the acquired pattern and the "amorphous" fit, and this refinement cycle was then repeated. This gave a satisfactory fit to the acquired diffraction pattern of the sample within the entire Q-range 1 to 3^{-1} Å. This decomposition scheme was applied to the diffraction pattern acquired at each η to find the crystallinity from

$$X_{c-\text{WAXS}} = \sum_\eta I'_{(110)} + I'_{(200)} + I'_{(020)} \Big/ \sum_\eta I'_{total} \qquad (3)$$
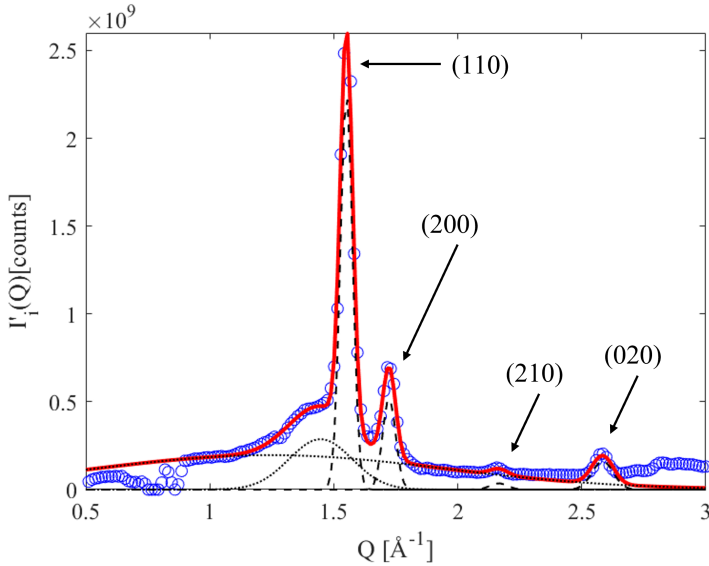
Fig. 4 Model of the diffraction pattern for the unstrained state in the Q-range 0.5 Å^{-1} to 3.0 Å^{-1}. The experimental data (circles) is fitted to the sum of six Gaussian functions (solid line). Four Gaussians represent the four peaks associated with the "crystalline" phase (dashed lines, indexed as peaks in Fig. 3). Two Gaussians (dotted lines) are used for fitting the "amorphous" phase and background.

We compared the fits at each external load step to determine the shifts in positions of the elements. The resulting shifts as function of η were subsequently used to determine the three strain components for each element, cf. Eq. 2. The shifts were found by cross-correlating the strained element with the corresponding unstrained element. The data points for both the strained and unstrained distributions were fitted with a smoothed spline intersecting all identified data points. The resulting intensity distributions for the strained state were cross-correlated with the unstrained reference measurement as illustrated in Fig. 5.

The well defined maximum of the cross-correlation curve is seen to correspond to the maximum position in the strained fit. We estimate the accuracy of this shift in position to be better than twice the distance between interpolation point, 5×10^{-6} Å^{-1}.

4 Results

4.1 Radiation damage test

As a representative result of the beam damage test, the time evolution of the most intense peak, (110), is shown in Fig. 6. For radiation exposures substantially exceeding that of the strain experiment, presented below, we saw no correlated evolution of the position nor the amplitude of the diffraction peaks.
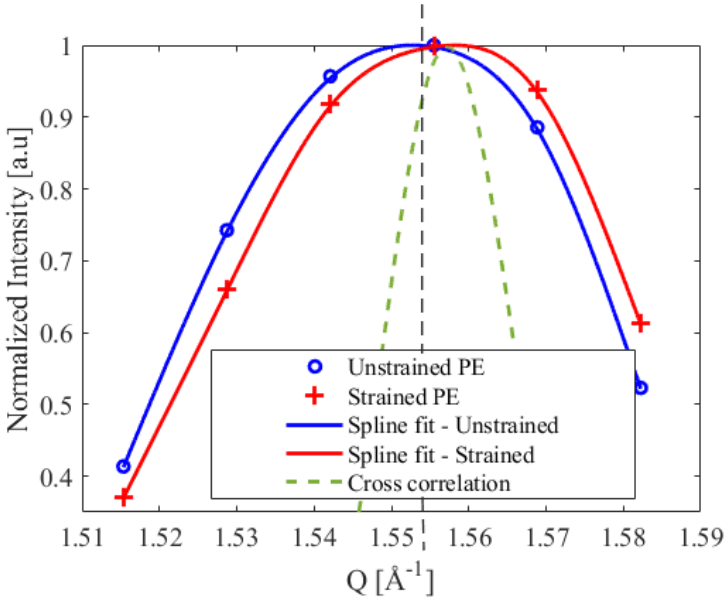
Fig. 5 Illustration of the cross correlation method. Experimental data for the (110) peak for unstrained (circles) and strained (crosses) PE are fitted with splines (blue and red line, respectively). The cross correlation between the two fits is calculated for different shift of the strained curve relative to the origin. The result is overlaid on the plot as a dashed curve. The dashed vertical line is a guide to the eye representing the maximum of the unstrained curve.

The measurement gives us a standard deviation of 2×10^{-4} for relative shift in position and 2×10^{-3} for relative intensity variation. We consider these numbers as an upper limit on the measurement uncertainties of the experiment. Note that the strain sensitivity may be improved by fits to the entire data set. Moreover, as the intrinsic accuracy of the cross correlation methods is more than an order of magnitude better, we conclude that the prime limitation on strain sensitivity in this experiment is signal-to-noise.

In the work by Coffey *et al.* [24] the ratio of crystalline mass for PE is shown to decrease in ionising radiation, whereby the peaks in the diffraction pattern shift position and decrease in amplitude. Coffey *et al.* subjected 100 nm foils of PE to radiation in an inert atmosphere with negligible changes, but in atmospheric oxygen a significant mass conversion was catalysed. Our samples were radiated in atmospheric conditions but the sample thickness was ≈ 2 mm and even with the high oxygen permeability of PE the conversion process may thus on average have been oxygen starved.

4.2 Initial texture

The as-received material was machined into a dogbone. This treatment will not influence the texture of the material except within a surface layer thin enough to not influence the diffraction signal from the bulk. The initial anisotropy is thus originating from the production process. In Fig. 7 the initial anisotropy
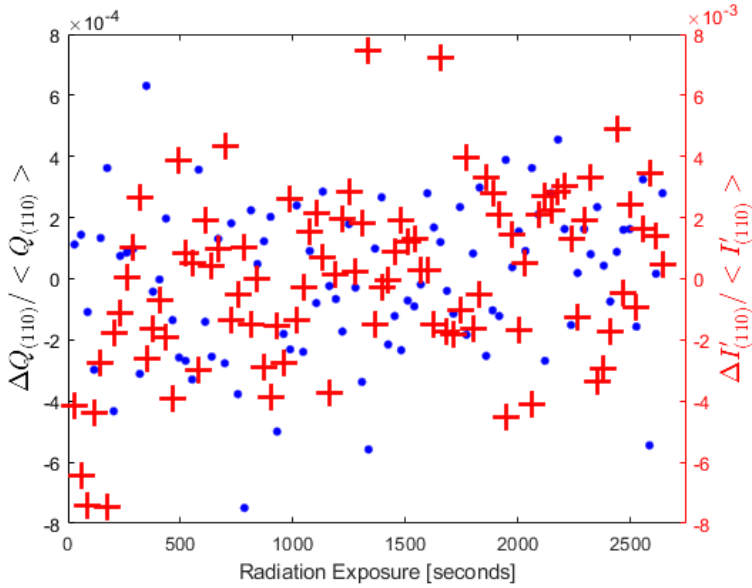
Fig. 6 Radiation damage test. Evolution of properties of the most intense diffraction peak, the (110) peak at $Q = 1.55$ Å^{-1}, as function of exposure time. Each data point represents the median of the results from 12 consecutive diffraction patterns acquired in the span of ≈ 22 seconds exposure including dead time. Blue dots correspond to the position of the peak relative to the average position. The standard deviation is 2×10^{-4}. The red crosses represent the relative amplitude of the peak. The standard deviation is 2×10^{-3}.

of the crystalline peaks are shown. The anisotropic part of the intensity I_A and the average baseline intensity I_{bl} are determined from a fit $I_{\eta,\epsilon_0} = I_{bl} + I_A \sin(\eta + \eta_0)$. The relative amplitude I_A/I_{bl} of this anisotropic part is shown in Fig. 7. The (020) peak exhibit the stronger anisotropy being twice that of the others. Not shown in the figure is the orientation of the initial texture. The initial orientations of (200) is orthogonal to the other peaks and (200) is aligned with the strain direction.

4.3 Strain evolution during tensile deformation

Initially we report on the evolution of strain within the crystalline phases. As an example, the resulting azimuthal variation in position of the (020) peak is shown in Fig 8 with external strain as parameter. An example of a fit of such curves to the expression in Eq. 2 is shown in Fig. 9. The sinusoidal variation is representative of the behaviour of all four "crystalline" peaks at all external loads. (In both Figs. 8 and 9 data points in the azimuthal range from 115° to 155° are excluded, as the beam stop shadows the detector in this range [1]).

The fit of the strain model to the data shown in Fig. 9 is seen as satisfactory. In the remainder of the paper we shall adopt the terminology of $\epsilon_\parallel$ for the axial strain, parallel to the direction of the applied strain, $\epsilon_\perp$ for the tangential

---

[1] For future reference, a beam-stop optimised for the size of the incident beam would be beneficial
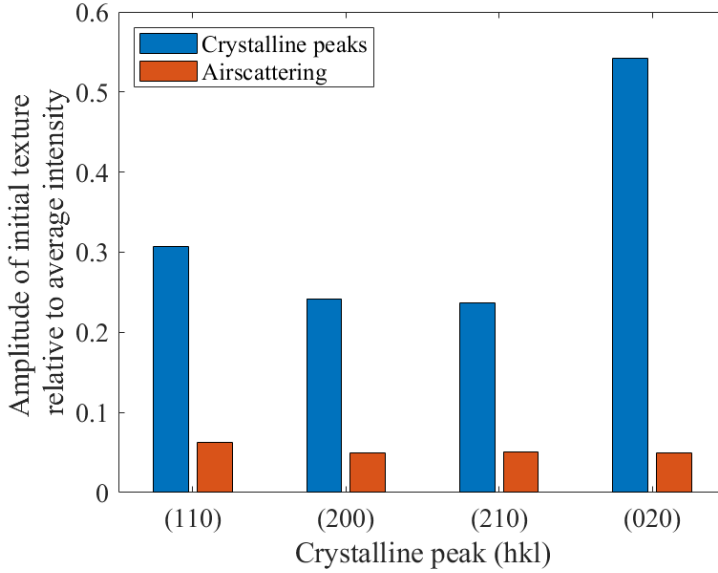
Fig. 7 The initial texture of the four crystalline peaks (blue bars). The azimuthal variation in intensity was fitted with a sine function. Shown is the amplitude of the sine function relative to the median intensity of the peak. To account for variations in detector efficiency and beam polarity the anisotropy - calculated in the same way - is also shown for the corresponding air diffraction signal (red bars).

strain in the perpendicular direction to the applied strain and ϵ_τ for the shear strain.

We note that the residuals, shown in Fig. 9 indicate the possible existence of an additional component to the diffraction model. We expect that a better correction of detector linearity would reduce this residual correlation. Furthermore since the beam width was only slightly smaller than the sample the assumption of an isotropic decrease in intensity for all η could be challenged for higher Q values.

The evolution of the resulting axial ($\epsilon_\parallel$), transverse ($\epsilon_\perp$) and shear (ϵ_τ) strains, are shown in Fig. 10 for the "crystalline" peaks. We call these mesoscopic strains as they are probed on a length scale of nanometers. We note that all components have the sign corresponding to a tensile strain. The mesoscopic and macroscopic strain are close to linearly correlated within the elastic strain range studied and it is therefore reasonable to fit a slope to each of these curves. From this we can determine the ratio $\epsilon_{meso}/\epsilon_{macro}$, where ϵ_{macro} is the macroscopic strain. We also determine the ratio $\epsilon_\perp/\epsilon_\parallel$ between mesoscopic strain perpendicular and parallel to the tensile direction. (Note that we in this experiment only had access to the perpendicular strain along the width dimension of the tensile sample – both for the mesoscopic and macroscopic measurements.)
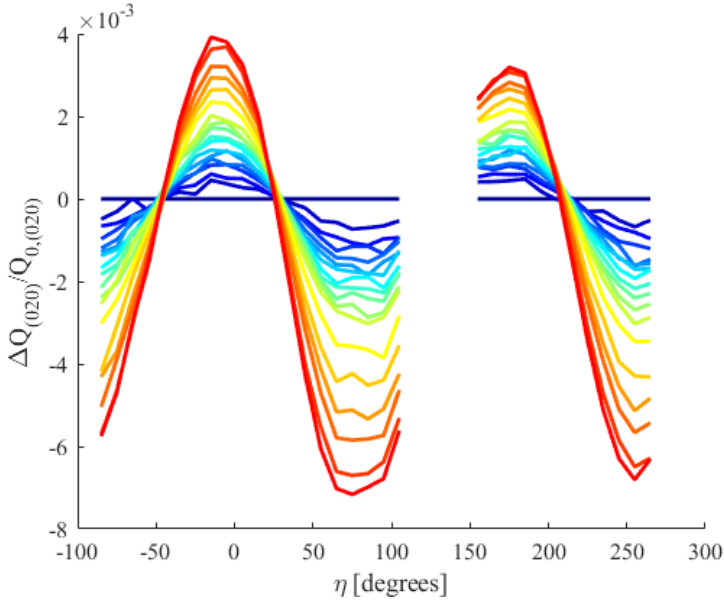
Fig. 8 Analysis of mesoscopic strain. The relative shifts in peak position of the (020) peak are shown as function of the azimuthal angle η. The curves represent increasing external strain (blue through red). Data in the η-range between $115°$ and $165°$ was removed due to interference of the beam-stop with the diffraction signal.
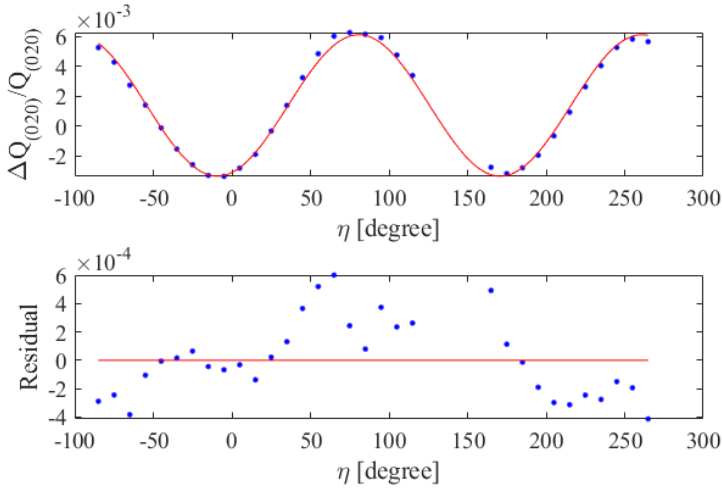

Fig. 9 Above: relative shift in Q of (020) as a function of azimuthal angle η for a global external strain of 6.2% (blue dots). The solid red line is a fit to the function in Eq. 2. Below: the residual when subtracting the fitted values from the experimental data.
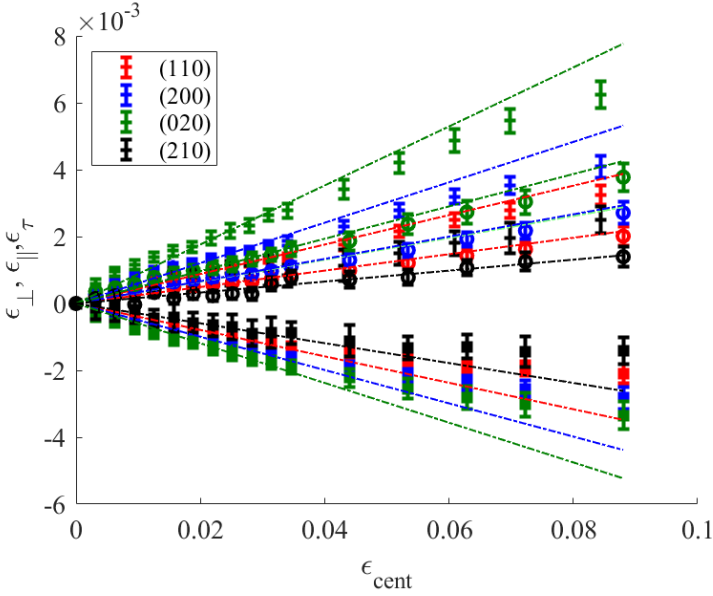
Fig. 10 Mesoscopic strain components for the "crystalline" phases as a function of external strain. The strain components $\epsilon_\perp$ (negative gradients and + markers), and $\epsilon_\|$ (positive gradient and + markers) and shear ϵ_τ (o markers) are shown with error bars corresponding to the RMS error of a fit to Eq. 2. The dashed lines represent fits of straight lines through (0, 0) to the data up to a strain of 3%.

Table 1 Table of mesoscopic mechanical parameters resulting from the linear fits in Fig. 10. The macroscopic value for the perpendicular strain are extracted from the optical camera. The macroscopic value for elongation has been adjusted according to the FE calculation in section 2.

	Q Å^{-1}	d Å	$\frac{\epsilon_{macro}}{\epsilon_{cent}}$	$\epsilon_\perp / \epsilon_\|$
Macroscopic				0.54 ± 0.1
(110)	1.46-1.63	4.1	30.4 ± 2.1	0.74 ± 0.06
(200)	1.64-1.82	3.6	22.2 ± 1.7	0.73 ± 0.06
(210)	2.1-2.2	3.0	41.9 ± 3.4	0.72 ± 0.06
(020)	2.48-2.68	2.4	15.2 ± 1.0	0.55 ± 0.04

In Table 1 the resulting mesoscopic mechanical parameters are listed. The uncertainties represent the 95% confidence intervals of the gradients in Fig. 10. For the confidence interval each data point is weighed inversely proportional to the errorbars in the same plot.

In this elastic regime the relation between mesoscopic and macroscopic strain are for all peaks a factor between 10 to 40 in correspondence with the notion that the elongation primarily give rise to entropic reconfiguration. Moreover, the ratio decreases continuously with increasing Q (and therefore with decreasing direct space distance r). In fact an inverse relationship:

$\epsilon_{meso}/\epsilon_{macro} \propto 1/Q$ describe the results well except for the peak (210). On the other hand the response of the peaks show no obvious correlation to crystallography. This in contrast to the classical strain response of crystalline materials where bond strength depends on crystallography (Schmidt factors).

From the FE calculation the ratio between strain perpendicular and along the drawing direction from geometric constraint should be 0.34 rather than the traditional macroscopic value found from the Poisson ratio , $\nu = 0.46$ [30]. Both values assumes an isotropic material and even with fairly high uncertainty on these numbers the results indicate this is not the case. To resolve this question, information from the depth dimension of our test specimen is required.

We conclude that the mesoscopic mechanical response of the "crystalline" phases is very different from that of a classical crystalline material due to the dominant role of the softer amorphous phase. When the material is elongated, part of the energy is absorbed in entropic reconfigurations of the polymers. This leads to different shells in the atomic pair correlation function responding differently, similar to the response of glasses [11]. It is however, intriguing that (within the crystalline phase) the shells become harder with increasing average distance r, while in the macroscopic limit, the response is soft. This is in direct contrast to the response of glasses.

4.4 Texture evolution during tensile deformation

It is relevant to compare the strain evolution at different length scales to the reorientation taking place at the same scales. To describe the evolution in orientation distribution we determine the intensity of each of the four tracked elements in the model for each of the segments defined in Eq. 1. Specifically, the intensity distribution of an element is integrated over the Q-range defined in Table 1. In Fig. 11 the variation with η is shown for each of the "crystalline" peaks at the maximum external strain.

A sinusoidal behavior is observed for all peaks corresponding to a change in intensity along and perpendicular to the external strain direction. The intensity for peaks (110), (200) and (210) increase for η perpendicular to the strain direction. The opposite is true for (020) where a (smaller) increase is observed for the parallel direction. The four peaks related to the orthorhombic phase all lie in the (hk0) plane and are consistent wrt. texture.

For each external strain level, curves similar to Fig. 11 are fitted to a sine function

$$I_{\eta,\epsilon}/I_{\eta,\epsilon_0} = I_{bl} + I_A \sin(\eta + \eta_0) \tag{4}$$

We use the ratio of the amplitude to the baseline I_A/I_{bl} as a measure of the texture evolution. The resulting texture evolution is presented in Fig. 12, for direct comparison with Fig. 10. The overall correlation between orientation change and external load is seen as a manifestation of increased chain alignment in the "crystalline" phases. For peaks (110) and (200) we note that the
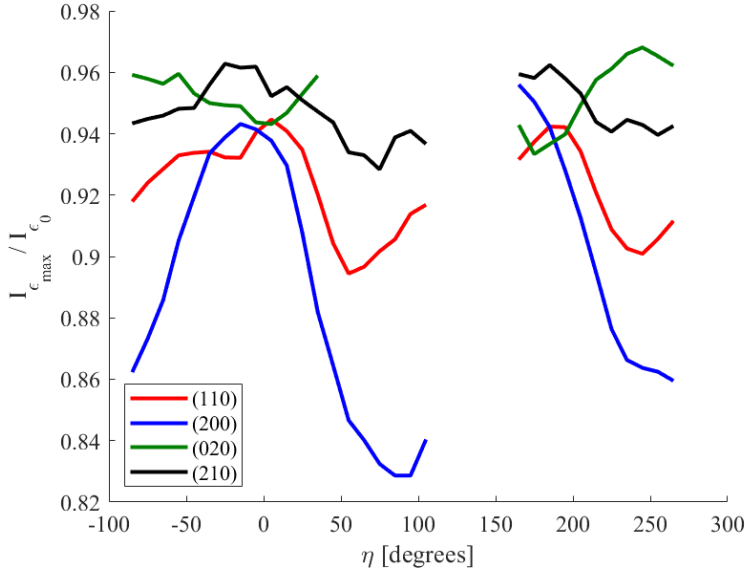
Fig. 11 Texture for the maximal external load. The relative intensity difference between fully strained and unstrained state for the 4 crystalline peaks is shown. The mean relative intensity is lower for all peaks due to a decrease in sample thickness.
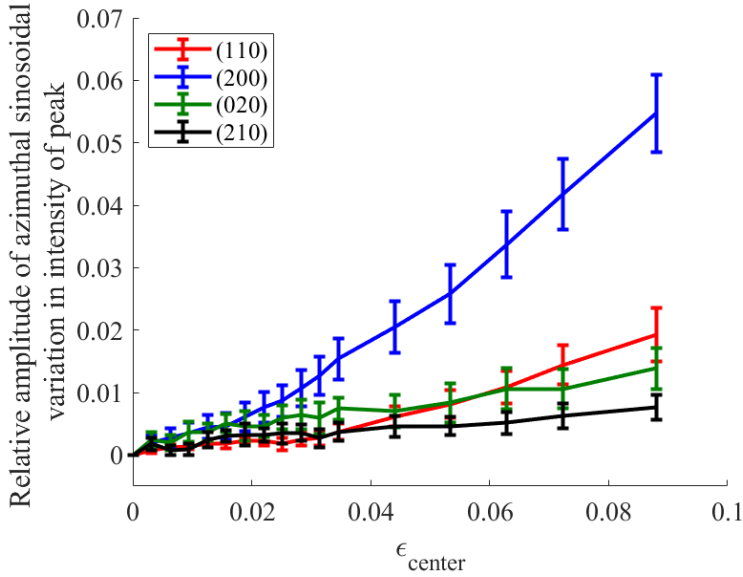

Fig. 12 Texture evolution. The relative amplitude of the sinosoidal variation of the intensity difference compared to zero external strain as a function of the external strain. This parameter corresponds to the shift in texture from the initial value as the polymer chains align in the direction of external strain. Errorbars represents the RMS error of a fit to Eq. 4.
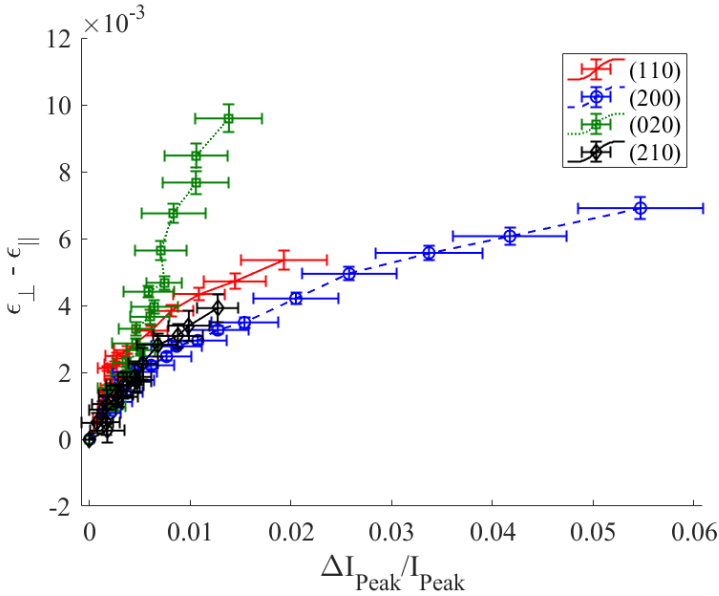
Fig. 13 Correlation of mesoscopic strain ϵ and texture for peaks 1 to 4. The difference between strain components, $\epsilon_\perp - \epsilon_\parallel$, and the anisotropy $I_A/I_b l$ is shown.

development of texture increases with Q, and therefore is inversely related to r. Hence, the innermost bonds appear to have more degrees of freedom to rotate. This surprising result mimics that of the strain variation with Q, see Table 1.

In the previous work on mesoscale strain in elastomers, a linear correlation was reported between the difference between the inter-chain strain components, and the inter-chain ordering – measured by the relative intensity difference of the first sharp diffraction peak at $(\eta = 0°)$ and $(\eta = 90°)$ [23] This is the anisotropy I_A/I_{bl}. The corresponding plot for the four "crystalline" peaks of PE is shown in Fig. 13. Evidently, there is no universal curve and at least three of the curves are clearly non-linear.

4.5 Crystallinity

The PE sample was measured with differential scanning calorimetry (DSC) to 50.1 % in the as-recieved state. In the Q-range of 0.5 to 2.5 Å we assess the integrated intensity of the diffraction signal for the crystalline and the amorphous phases respectively based on the decomposition model illustrated in Fig. 4. Determined in this way, initially the crystalline phase comprise 50.5 % of the total material.

The evolution of this x-ray measured crystallinity ratio with the external load is shown in Fig. 14. As expected [31] the crystalline fraction are constant up to the end of the linear regime and afterwards decreases very slightly with load and at a rate that is much lower than the corresponding evolution in texture.
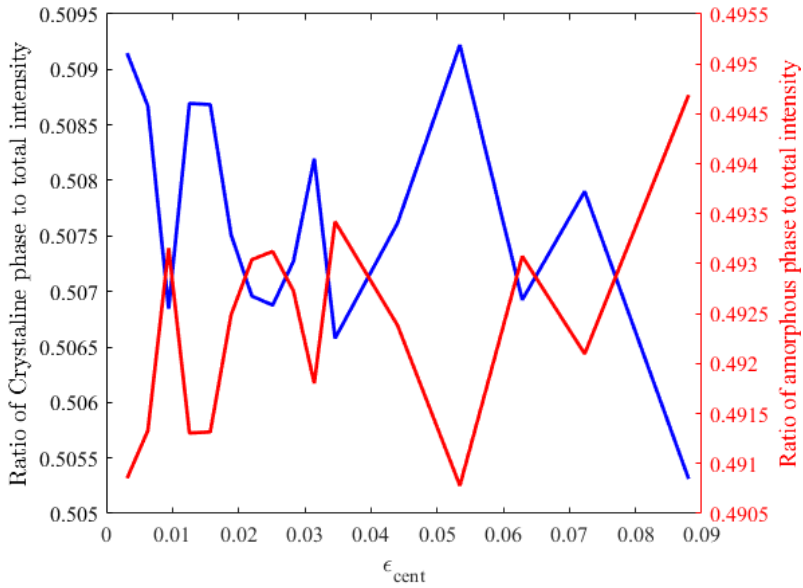
Fig. 14 Evolution in crystallinity with external strain. Shown in blue is the ratio of the integrated intensity associated with the crystalline phases and the total integrated intensity. Shown in red is the corresponding curve for the amorphous phase. The crystalline phase intensity is determined as the total integrated intensity of the Gaussian peak fits from the decomposition.

4.6 Data analysis approach

The method presented offers a unique possibility for testing micro-mechanical models of the response of thermoplasts like PE on several length scales. However, for basic research we would recommend to use an atomic model to interpret the diffraction data and an improved data analysis pipeline, similar to the previous work on mesoscale strain in inorganic glasses [11] and elastomers [23]. Deriving direct space correlation functions and performing a PDF analysis of the data is relevant, and would give direct information on the evolution of interatomic bond-length as well as a better separation of the two phases. Knowing the molecular structure of the two phases one can also provide more detailed and accurate models that predict the diffracted intensity pattern. Likewise Legendre polynomials provide a better description of the texture evolution [23].

For use in engineering, however, the present data analysis approach is well suited: the analysis of shifts of peaks in Q-space does not require any *a priori* knowledge of the molecular structure nor advanced data analysis tools (beyond cross correlation). Hence, it seems likely that it can find application also for less ideal instrumental settings and for unknown materials.

4.7 Applicability of the mesoscale strains as a tool in engineering

A motivation for this work is the perspective of using the mesoscale strains as a local strain gauge for inspection and for interfacing with mechanical modelling. The fact that within the external strain range studied, the response is linear on all length scales, and for both phases implies that we can assume that any of these probes is proportional to the "relevant" length scale for e.g. the initiation of failure. For PE it would therefore be natural to focus on the shift of the most intense peak. It is also noteworthy that the texture evolution is not linear, and hence a less likely candidate as a proxy for determining the local macroscopic strain.

The accuracy of the mesoscopic strain determination was determined to be 5×10^{-6} in the absence of signal-to-noise issues. Moreover, the uncertainty on strain arising from a single segment was determined in section 4.1 to be 2×10^{-4}. There is strong evidence from strain characterisation of other materials that this error will be "quenched" when performing the joint fit to all segments, by an amount of approximately $\sqrt{36}$. From this we make the tentative conclusion that a sensitivity of mesoscopic strains of order 3×10^{-5} is within reach. Using the correlation between mesoscopic and macroscopic strain provided in table 1, the sensitivity to local macroscopic strain becomes below 10^{-3}. This is an excellent result, that however eventually need verification by definition and use of strain scanning standards.

As an input to a mechanical model the results presented may be insufficient as the strain of the amorphous component is absent and not all components were probed for the crystalline phase. We did perform a similar analysis to that presented in sections 4.2-4.4 for the amorphous component, and found indications of a load sharing. However, issues with the beamstop (and also a too primitive model of $S(Q)$ for this phase) implied that the uncertainties on the results are too high. We are confident though, that the strain evolution of the amorphous phase can be found from optimised experiments.

The generalisation to provision of all strain components is straight forward and only requires repeating the study at 2 or more projections. The relevant rotation is readily available at any instrument that support diffraction or (diffraction) tomography.

4.8 Outlook

Similar to previous work on crystals and glasses, the next step is to extend the characterisation to mapping of 2D or 3D strain fields by scanning slits [32], wires [9], micro-channel plates [33] or coded apertures through the diffracted signal. Such 3D maps would in a unique way facilitate comparison with 3D micro-mechanical modelling, for guidance and validation of the models.

The prospect of application are wide ranging and includes studies of composite materials to understand structural integrity and degradation, materials

for high voltage applications to identify regions with decreased insulation capabilities and soft robotics utilised in e.g prosthetics. Stress and strain fields are hard to identify inside complex structures using conventional measurement techniques and the challenges cover many length scales. Medico products based on polymers often rely on build-in stresses in its application. Contrary to this and at a larger scale, adhesive joints of cm thicknesses in wind turbine blades can develop local damage due to build in stresses [34].

5 Conclusion

We have presented a simple analysis scheme to extract local strain components with high accuracy from semicrystaline polymers. In the elastic strain regime of PE we have shown that the correlation between average strain and local mesoscopic strain is linear at all length scales.

The method simultaneously extracts the evolution of texture. For PE the texture exhibited a nonlinear response to the externally applied strain making it less suitable as a proxy for describing the local strain in engineering applications.

This work also makes it clear that the mesoscopic response to the stress field is very dependent on length scale. For polyethylene the response for (020) was 2.1 times higher than the otherwise most prominent component the (110) peak. To obtain quantitative measurements of the local macroscopic strain field from this method for a certain (class of) materials it is thus necessary to have performed a calibration experiment to understand the mesoscopic response and to identify the most sensitive component.

Declarations

- Conflict of interest The authors have no conflicts of interest to declare that are relevant to the content of this article.
- Ethics approval Not applicable
- Consent to participate Not applicable
- Consent for publication Not applicable
- Availability of data and materials Data is avaiable upon request
- Code availability Code is not available at this time
- Authors' contributions Not applicable

References

[1] Noyan, I.C., Cohen, J.B.: Residual Stress. Springer, Berlin (1987)

[2] Fitzpatrick, M., Lodini, A.: Analysis of Residual Stress by Diffraction Using Neutron and Synchrotron Radiation. Taylor and Francis, London (2003)

[3] Kirkpatrick, P., Baez, A.V., A., N.: Geometrical optics of grazing incidence reflectors. Phys Rev. **73**, 535–536 (1948)

[4] Snigirev, A., Kohn, V.G., Snigireva, I.I., Lengeler, B.: A compound refractive lens for focusing high-energy x-rays. Nature **384**, 49 (1996). https://doi.org/10.1038/384049a0

[5] Pfeiffer, F., David, C., Burghammer, M., Riekel, C., T., S.: Two-dimensional x-ray waveguides and point sources. Science **297**, 230–234 (2002). https://doi.org/10.1126/science.1071994

[6] Morgan, A.J., Prasciolu, M., Andrejczuk, A., Krzywinski, J., Meents, A., Pennicard, D., Graafsma, H., Barty, A., Bean, R.J., Barthelmess, M., Oberthuer, D., Yefanov, O., Aquila, A., Chapman, H.N., Bajt, S.: High numerical aperture multilayer laue lenses. Sci. Rep. **5**, 9892 (2015). https://doi.org/10.1038/srep09892

[7] Reimers, W., Pyzalla, A., Broda, M., Brusch, G., Dantz, D., Schmackers, T., Liss, K., Tschentscher, T.: The use of high-energy synchrotron diffraction for residual stress analyses. J. Mater. Sci. Lett. **18**, 581–583 (1999)

[8] Poulsen, H.F., Nielsen, S.F., Lauridsen, E.M., Schmidt, S., Suter, R., Lienert, U., Margulies, L., Lorentzen, T., Juul Jensen, D.: Three-dimensional maps of grain boundaries and the stress state of individual grains in polycrystals and powders. Journal of applied crystallography **34**(6), 751–756 (2001). https://doi.org/10.1107/S0021889801014273

[9] Larson, B.C., Yang, W., Ice, G.E., Budai, J.D., Tischler, J.Z.: Three-dimensional x-ray structural microscopy with submicrometre resolution. Nature **415**, 887–890 (2002). https://doi.org/10.1038/415887a

[10] Simons, H., King, A., Ludwig, W., Detlefs, C., Pantleon, W., Schmidt, S., Stöhr, F., Snigireva, I., Snigirev, A., Poulsen, H.F.: Dark field x-ray microscopy for multiscale structural characterization. Nat. Commun. **6**, 6098 (2015). https://doi.org/10.1038/ncomms7098

[11] Poulsen, H.F., Wert, J.A., Neuefeind, J., Honkimäki, V., Daymond, M.: Measuring strain distributions in amorphous materials. Nature Mater. **4**,

33–36 (2005). https://doi.org/10.1038/nmat1266

[12] Lunt, A.J.G., Chater, P., Korsunsky, A.M.: On the origins of strain inhomogeneity in amorphous materials. Sci. Reports **8**, 1574 (2018). https://doi.org/10.1038/s41598-018-19900-2

[13] Guevara-Morales, A., Figueroa-López, U.: Residual stresses in injection molded products. Journal of Materials Science **49**(13), 4399–4415 (2014). https://doi.org/10.1007/s10853-014-8170-y

[14] Pepin, J., Gaucher, V., Rochas, C., Lefebvre, J.M.: In-situ SAXS/WAXS investigations of the mechanically-induced phase transitions in semicrystalline polyamides. Polymer **175**, 87–98 (2019). https://doi.org/10.1016/J.POLYMER.2019.04.073

[15] Xiong, B., Lame, O., Chenal, J.M., Rochas, C., Seguela, R., Vigier, G.: In-situ SAXS study of the mesoscale deformation of polyethylene in the pre-yield strain domain: Influence of microstructure and temperature. Polymer **55**(5), 1223–1227 (2014). https://doi.org/10.1016/J.POLYMER.2014.02.004

[16] Humbert, S., Lame, O., Chenal, J.M., Rochas, C., Vigier, G.: Small strain behavior of polyethylene: In situ SAXS measurements. Journal of Polymer Science Part B: Polymer Physics **48**(13), 1535–1542 (2010). https://doi.org/10.1002/POLB.22024

[17] Millot, C., Séguéla, R., Lame, O., Fillot, L.A., Rochas, C., Sotta, P.: Tensile Deformation of Bulk Polyamide 6 in the Preyield Strain Range. Micro-Macro Strain Relationships via in Situ SAXS and WAXS. Macromolecules **50**(4), 1541–1553 (2017). https://doi.org/10.1021/acs.macromol.6b02471

[18] Asp, L.E., Berglund, L.a., Talreja, R.: A criterion for crack initiation in glassy polymers subjected to a composite-like stress state. Composites Science and Technology **56**(11), 1291–1301 (1996). https://doi.org/10.1016/S0266-3538(96)00090-5

[19] Zobeiry, N., Forghani, A., Li, C., Gordnian, K., Thorpe, R., Vaziri, R., Fernlund, G., Poursartip, A.: Multiscale characterization and representation of composite materials during processing. Philosophical Transactions of the Royal Society A: Mathematical, Physical and Engineering Sciences **374**(2071) (2016). https://doi.org/10.1098/rsta.2015.0278

[20] Nishida, M., Kitamura, M., Hanabusa, T., Matsue, T.: X-ray Residual Stress Measurement of Fiber Reinforced Plastic Composite. Journal of Solid Mechanics and Materials Engineering **4**(8), 1178–1185 (2010). https://doi.org/10.1299/jmmp.4.1178

[21] Hughes, D.J., Heeley, E.L., Curfs, C.: A non-destructive method for the measurement of residual strains in semi-crystalline polymer components. Materials Letters **65**(3), 530–533 (2011). https://doi.org/10.1016/j.matlet.2010.10.046

[22] Schneider, K.: Investigation of structural changes in semi-crystalline polymers during deformation by synchrotron X-ray scattering. Journal of Polymer Science Part B: Polymer Physics **48**(14), 1574–1586 (2010). https://doi.org/10.1002/polb.21971

[23] Neuefeind, J., Skov, A.L., Daniels, J.E., Honkimäki, V., Jakobsen, B., Oddershede, J., Poulsen, H.F.: A multiple length scale description of the mechanism of elastomer stretching. RSC Adv. **6**, 95910 (2016). https://doi.org/10.1039/C6RA22802J

[24] Coffey, T., Urquhart, S.G., Ade, H.: Characterization of the effects of soft X-ray irradiation on polymers. Journal of Electron Spectroscopy and Related Phenomena **122**(1), 65–78 (2002). https://doi.org/10.1016/S0368-2048(01)00342-5

[25] Howard, S.: Materials Data Book. Cambridge University Engineering Department, Cambridge, UK (2003)

[26] Van Driel, T.B., Kjær, K.S., Hartsock, R.W., Dohn, A.O., Harlang, T., Chollet, M., Christensen, M., Gawelda, W., Henriksen, N.E., Kim, J.G., *et al.*: Atomistic characterization of the active-site solvation dynamics of a model photocatalyst. Nature communications **7**(1), 1–7 (2016). https://doi.org/10.1038/ncomms13678

[27] Bunn, C.W.: The crystal structure of long-chain normal paraffin hydrocarbons. The "shape" of the CH2 group. Transactions of the Faraday Society **35**, 482–491 (1939)

[28] Rice, J.R.: Solid Mechanics. Harvard University, Boston (2010)

[29] Monar, K., Habenschuss, A.: Modeling the principal amorphous halo in quiescent melts of polyethylene and ethylene copolymers using wide-angle X-ray scattering and its implications. Journal of Polymer Science Part B: Polymer Physics **37**(24), 3401–3410 (1999). https://doi.org/10.1002/(SICI)1099-0488(19991215)37:24$\langle$3401::AID-POLB3/$\rangle$$3.0.CO;2-Y

[30] CROW: Chemical Retrieval on the Web (CROW) - Polymer Properties Database. Accessed = 2020-07-02 (2020). https://polymerdatabase.com/polymerphysics/PoissonTable.html

[31] Chang, B., Schneider, K., Xiang, F., Vogel, R., Roth, S., Heinrich, G.: Critical Strains for Lamellae Deformation and Cavitation during Uniaxial

Stretching of Annealed Isotactic Polypropylene. Macromolecules **51**(16), 6276–6290 (2018)

[32] Lienert, U., Martins, R., Grigull, S., Pinkerton, M., Poulsen, H.F., Kvick, Å.: High spatial resolution strain measurements within bulk materials by slit-imaging. Mater. Res. Soc. Symp. Proc. **590**, 241–246 (2000). https://doi.org/10.1557/PROC-590-241

[33] Wroblewski, T., Breuer, D., Crostack, H., Fandrich, F., Gross, M., Klimanek, P.: Mapping in real and reciprocal space. Mater. Sci. Forum **278-281**, 216–220 (1998). https://doi.org/10.4028/www.scientific.net/MSF.278-281.216

[34] Jørgensen, J.B., Sørensen, B.F., Kildegaard, C.: Tunneling cracks in full scale wind turbine blade joints. Engineering Fracture Mechanics **189**, 361–376 (2018). https://doi.org/10.1016/j.engfracmech.2017.11.016

Multiscale characterisation of strains in semicrystalline polymers

Ulrik L. Olsen[1*], Mads G. Laursen[1], Piotr S. Mazurek[2], Jan Kehres[1], Lars P. Mikkelsen[3], Anne L. Skov[2] and Henning F. Poulsen[1]

[1*]Department of Physics, Technical University of Denmark, Fysikvej 1, Kgs. Lyngby, 2800, Denmark.
[2]Department of Chemical Engineering, Technical University of Denmark, Søltofts Plads 288A , Kgs. Lyngby, 2800, Denmark.
[3]Department of Wind Energy, Technical University of Denmark, Frederiksborgvej 399, Roskilde, 4000, Denmark.

*Corresponding author(s). E-mail(s): ullu@dtu.dk;

Abstract

A nondestructive probe for mapping elastic strains within polymers would be an asset for materials engineering: for validation of mechanical models and for understanding damage nucleation. As a step towards this aim we demonstrate an X-ray wide angle diffraction methodology probing strain tensor components on mesoscopic length scales, in the range 3-50 Å. We demonstrate its use on a 50 % semi-crystalline polyethylene sample subjected to tensile straining up to 8.8 %. The mesoscopic strains derived for the crystalline phase scale linearly with the macroscopic strain, in contrast to the crystallised volume fraction and the texture evolution. In the crystalline phase, the material becomes softer and exhibit a larger degree of alignment with decreasing distance in direct space. The inherent strain sensitivity is 10^{-5}. The prospect of 3D mapping of local strain and stress tensors is discussed.

Keywords: X-ray imaging, X-ray diffraction, Polymers, Strain

1 Introduction

Elastic strain plays a crucial role in the structural organisation of crystalline specimens. Examples are the formation of nanodots in semiconductors, dislocation structures in plastically deformed metals and the phase morphology generated by solid-state phase transformations. In terms of engineering, control of the elastic strain is vital to increase product lifetime. X-ray and neutron diffraction methods [1, 2] allow determination of the elastic strain tensor non-destructively as a function of (x,y,z) position within the specimen. Furthermore, using synchrotron radiation and x-ray optics, the dimension of the X-ray beam can be varied from 10 nm to 1 mm [3–6]. This has led to the establishment of a number of methods for strain scanning on the engineering scale [2, 7] as well as on the scale of the (embedded) grains and sub-grains [8–10].

In Poulsen *et al.* [11] it was demonstrated that wide angle diffraction with hard x-rays can be used also for characterising bulk stress and strain fields in glasses. The strain accuracy is approximately 10^{-4}. This approach has been used extensively for studies of inorganic glasses [12]. In these studies it is typically found that the macroscopic response is less stiff than the atomic next-neighbour bonds because of structural rearrangements at the scale of 4-10 Å.

To our knowledge, characterisation of strain in amorphous polymers with diffraction methods has not been reported and even for semi-crystalline polymers results are precious few. Stress characterisation is therefore largely based on destructive techniques, or optical methods relying on changes in the refractive index with stress, both with limited applicability [13]. Several studies [14–17] establishes that a constant relationship $\epsilon_{local}/\epsilon_{macro}$ between the strain measured with SAXS and the externally applied strain exist in the pre-yield elastic strain domain. For PE at 25^oC specifically $\epsilon_{local}/\epsilon_{macro}$ is 0.5 even as the crystallinity changes although the ratio changes slightly with temperature and for other materials. But rather than a method for mapping local strain the investigations are investigating the influence of straining on the lamellae stacks and the spherulites in semicrystalline polymers to understand the structural behaviour. The relative scarcity of non-destructive bulk investigations is remarkable, as the impact of understanding strain and stress in polymers within materials science and engineering parallels that of crystalline materials. As examples, polymers are extensively used as adhesive joints and as matrix material in fibre reinforced composites, both with major applications in the aerospace, automotive and wind energy sector. Residual stresses developed during the manufacturing process will often have undesired impact on the mechanical performance [18, 19] such as reduction of fatigue lifetime, distortion of shape and lower ductility.

For thermoplasts we are aware of three X-ray diffraction based studies. Nishida *et al.* reported strain behaviour in fibre reinforced high density polyethylene (HDPE) using the sine-square-psi method on one diffraction peak [20]. Hughes *et al.*, also studied a single peak of HDPE but without an analysis of the texture evolution 2011 [21]. Schneider performed a study of injection

molded polypropylene at strains up to 800 % using both small angle and wide angle diffraction [22].

It is characteristic of these publications that analysis schemes for strain characterisation of classical crystalline materials were applied. However, in contrast to metals or ceramics we lack a microscopic understanding of the generation of strain in polymers, and even a definition. The energy absorbed during loading is primarily transformed into entropic terms, and in a tensile experiment the pair correlation function between atoms - which is what is measured by wide angle x-ray scattering (WAXS) - will therefore change much less with increasing elongation than is the case for hard materials, such as the crystals and inorganic glasses. Moreover, the strain is likely to vary with distance in the mesoscopic 3-50 Å range, leading to corresponding variation of the WAXS signal with distance in reciprocal space, $|\vec{Q}|$. In a semicrystalline polymer the process is further complicated by possible loadsharing with the amorphous phase, and by texture evolution. As a result the measurement of strain based on wide angle diffraction may not be linearly related to the external load, and will depend on which mesoscopic length scale one probes.

In this article we aim to make a comprehensive study of WAXS based strain analysis to a prototype thermoplast, of relevance for engineering: polyethylene (PE). We introduce the above mentioned methodology for characterising glasses [11, 23], and show it provides an excellent strain resolution. Using this we study simultaneously the strain and texture evolution during an *in situ* tensile experiment, as a function of mesoscopic length scale. We believe such data is a good starting point for deriving a micromechanical model of strain in thermoplasts. In this article, however, the focus is on elucidating if and how x-ray diffraction can be used by engineers for mapping the strain tensor in thermoplasts. From the strain tensor the stress tensor can be determined by means of Hooke's law assuming a linear elastic material response.

2 Experimental set-up

The *in-situ* experiment took place at beamline BL04B2 at the SPring-8 synchrotron facility. A schematic of the set-up is shown in Fig. 1. The energy of the incident radiation was 61.4 keV. The X-ray beam was monochromatised and focused in the horizontal plane by means of a Si 220 bent crystal monochromator. The samples were illuminated with a 3×3 mm^2 beam in transmission geometry. The acquisition time of the diffraction patterns was on average 120 s. The area detector used was a XRD1621XN ES CT-grade detector from Perkin-Elmer (now Varex Imaging) with 2048×2048 pixels and an active area of 409.6×409.6 mm^2. With the detector positioned 329.5 mm from the sample, the transmission set-up allowed the acquisition of data within a Q-range of 0.5 to 6.2 Å^{-1}. The detector was positioned asymmetrically relative to the direct beam such that the Q-range was extended in the upwards direction (in the direction $\eta = 0$, cf Fig. 1). The beam stop shadowed for a region of the image; we use a software mask to disregard the signal from this region.
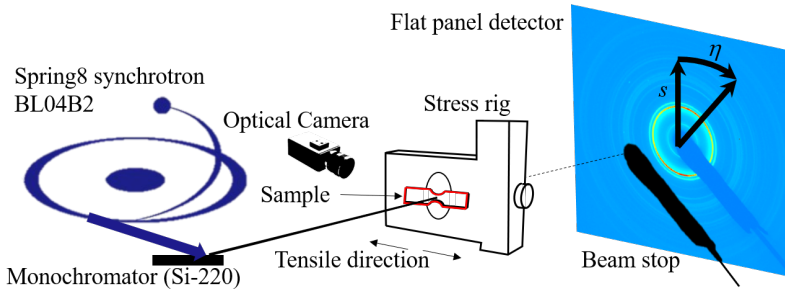
Fig. 1 Schematic diagram showing the high-energy X-ray diffraction setup used in the experiment. The sample was fixed in the stress rig at the side facing the detector, which is contrary to the schematic. An optical video sensor was mounted at an angle to capture optical images of the position of the sample during straining. The image on the 2D detector is an example of raw data with indication of zero points of the polar coordinates (s,η) used.

The material of choice was PE, acquired from Carlson & Möller, Helsingborg. The degree of crystallinity was determined using differential scanning calorimeter (DSC) Discovery from TA Instruments, USA. The specimens were exposed to heating/cooling at a rate of 10 °C min^{-1} in nitrogen atmosphere. The DSC measurement was repeated three times and results were averaged to give a final crystallinity of $50.1 \pm 0.5\%$.The density was determined using a pycnometer bottle and liquid immersion to be 0.922 g cm^{-3}. The sample was machined to a tensile test dog-bone with dimension 31mm×7mm×2.1mm (height, width, depth); the waist of the dogbone was machined as a round cutout 6.7 mm long and narrowing the test piece to 3.1 mm in the centre of the cutout making the smallest cross section area of the sample 6.5mm^2. The specimen geometry is also shown in Fig. 2.

Ionising radiation is known to influence the structure of polymers, giving rise to beam damage, see e.g. [24]. However, traditionally x-ray diffraction experiments are performed at much lower energies with a less favourable ratio between diffraction and absorption cross sections than in this experiment. In many cases the beam is furthermore poly-chromatic and originates from a small volume. The use of a high energy, monochromatic beam and a large sample volume at BL04B2 is assumed to make beam damage of the sample negligible. We performed a test of this assumption on a separate PE sample mounted in the same way as in the *in situ* experiment. Here diffraction patterns were continuously acquired during radiation for 2500 seconds. The acquisition time of each pattern was 1 second. The median of 12 exposures was used for each data point and including dead time each data point corresponds to 22 seconds of exposure.

For the tensile straining the dogbone sample was mounted in a Linkam TST350 thermomechanical tensile testing cell. The load stage was equipped with a 200 N load cell and self-centring grips which assured that the applied load was uniaxial. The load resolution of the cell was 10 mN, strain rates were 50 μm s^{-1} and strain resolution was specified to 1 μm.

During the experiment, the specimen was stretched in 11 steps of 40 μm, four steps of 120 μ m and two steps of 200μ m. Between each step the specimen was allowed to relax for $\approx$ 3 minutes; the stress values determined directly after each step has been used in the subsequent analysis. The drawing began from an unloaded state with a distance of 7.9 mm between stress rig grips and continued until an average elongation of 7.4% was achieved. At this point the specimen slipped in the grips. This final point is excluded from the data analysis, as well as the initial points until a positive stress on the sample was achieved.

Modelling the test-geometry using a 3-dimensional finite element model, a relation between the overall average strain, ϵ_a measured between the grips and the average strain, ϵ_{cent}, in the 3×3^{-2} mm central illuminated gauges section can be calculated. Taking an linear elastic isotropic material with $E = 203$ MPa and $\nu = 0.46$, a relation of $\epsilon_{cent} = 1.41\epsilon_a$ is found. In addition, the centre region will due to the constraining effect in the width direction in the notched region, have a lower apparent Poisons ratio given by $\nu_{cent} = 0.34\nu$.

Based on the average strain in the centre part of the test-geometry and the stresses calculated by the applied load divided by the narrow 3.1×2.1 mm^2 cross-section, the recorded macroscopic stress-strain curve is reproduced in Fig. 2 with the strain steps indicated. A linear fit between 0% and 6.2% was used to determine macroscopic Young's modulus of 203 MPa in correspondence with the typical range of LDPE of 100-350 MPa [25].

3 Data analysis scheme

The data analysis follows the procedure established in Neufeind *et al.* [23] - it is illustrated in Figs. 1 and 3. The nearly circular symmetric diffraction patterns are parameterised with respect to polar coordinates (s,η), see Fig. 1. In this work we divided the η-range of $[0\ 2\pi]$ into 36 segments. Hence for $i = 1...36$ the i'th segment starts at $\eta_i = (i-1) * 2\pi/36$. For each segment the intensity distribution

$$I_i'(Q) = \int_{\eta_i}^{\eta_i+\pi/18} I(Q, \eta)d\eta; \quad i = 1..36 \tag{1}$$

is determined, with $Q = Q(s)$ defined by Bragg's law. An example of such an intensity distribution $I_i'(Q)$ is shown in Fig. 3.

As a part of the conversion from raw data to 1D diffraction pattern the influence of the detector was corrected in terms of solid angle coverage and efficiency following the methodology in van Driel *et al.* [26]. The sample cross section decreases during strain according to the Poisson's ratio of the material leading to a decreasing diffraction interaction volume. In our analysis we assume that this effect decreases intensity isotropically and thus uniformly for all $I_i'(Q)$. This assumption is valid when the sample is much larger than
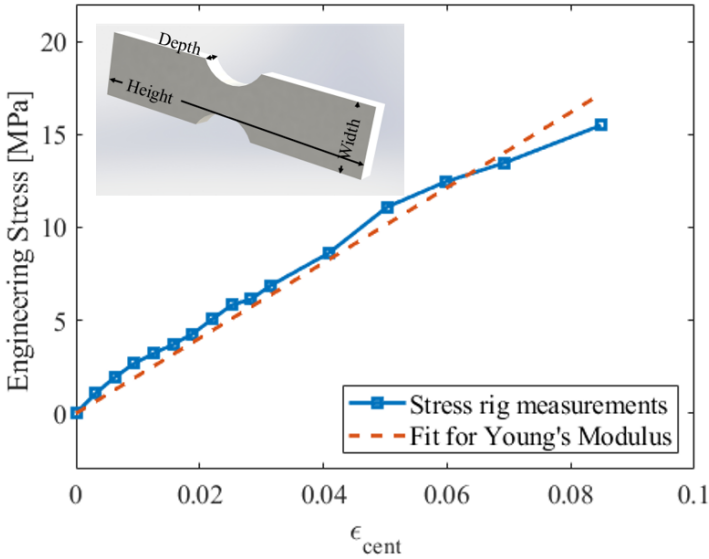
Fig. 2 The macroscopic stress-strain curve for the PE dogbone sample acquired during the experiment. The stress data is taken from the stress sensor directly as the strain step was reached disregarding any subsequent relaxation of stress before the next strain step. The strain was determined from the cumulative sum of steps taken from the operational interface since the strain from the images acquired with the optical camera had a considerably lower measurement precision. The insert shows the PE dogbone with dimensions indicated.

the beam in both directions perpendicular to the beam direction and when diffraction angles are small.

The diffraction pattern in Fig. 3 exhibits several distinct maxima, that we will associate with the "crystalline" phase. Following Bunn [27] and Nishida *et al.* [20] we identify the peaks (110), (200),(210) and (020) in Fig. 3 as belonging to an orthorhombic structure, with space group 62 (Pnma). From these data we find $a = 7.24$ Å and $b = 4.88$ Å. In comparison, Nishida *et al.* reported 7.4 Å and 4.9 Å for the same unit cell parameters for HDPE.

For each of these four main peaks of the "crystalline" phase and for each $I'_i(Q)$ the relative shift in position of the peak is determined with respect to the unloaded situation (subscript 0): $q_i = \frac{Q_i - Q_{i,0}}{Q_{i,0}}$. In the small strain limit q_i is the inverse of the corresponding strain in direct space $\epsilon_i = -q_i$. We have conservatively taken the threshold strain where this assumption holds to be 3%. To increase sensitivity, this analysis is performed by treating the unloaded distribution in the vicinity of the peak as a correlation function. The angular variation of the relative shifts ϵ_i thus obtained is fitted to the expression:

$$\epsilon_i = \epsilon_{11} \sin^2(\eta_i) + 2\epsilon_{12} \sin(\eta_i)\cos(\eta_i) + \epsilon_{22} \cos^2(\eta_i) \ \ i = 1..36 \qquad (2)$$
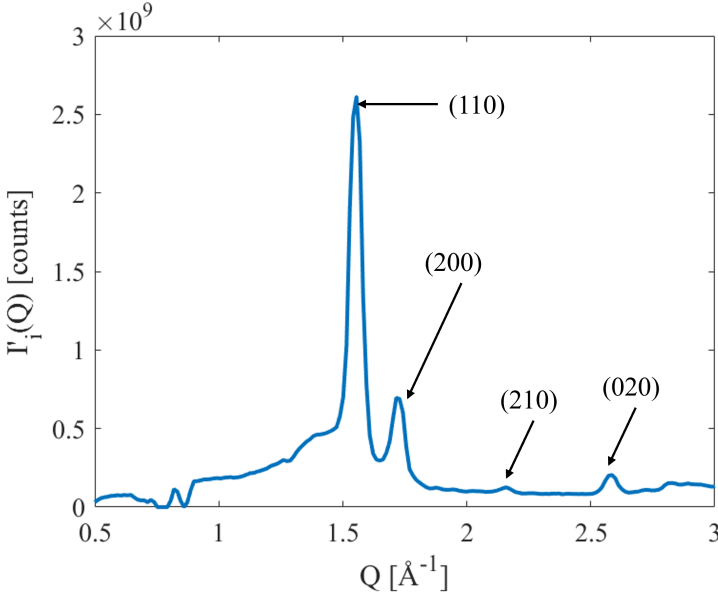
Fig. 3 Data analysis procedure. The raw data shown on the detector in Fig.1 are integrated azimuthally within 36 segments, an example of which ($\eta = 0$) is shown with the abscissa in units of Q. Four of the peaks belong to an orthorhombic phase - these are marked according to Miller indices.

As a result, three components of the strain tensor are determined: the axial (ϵ_{11}), tangential (ϵ_{22}) and in-plane shear component (ϵ_{12}). The expression comes from regular solid mechanics definition of the nine strain components [28]. The other strain components that are not in the plane perpendicular to the incoming beam can be determined from an experiment where the specimen is rotated around an axis perpendicular to the incoming beam.

To derive information on the mechanical properties we made a simple model of the diffraction intensity for PE as comprised of contributions from an "amorphous" phase and from the crystalline phase. As illustrated in Fig. 4 the crystalline part is represented by the four main peaks modelled as Gaussians. Following Monar *et al.* [29] in a crude approximation we model the amorphous phase by a Gaussian distribution. The model for the amorphous phase was fitted to the residual of the acquired pattern and the initial crystalline fit. The crystalline fit was then refined by fitting the model to the residual of the acquired pattern and the "amorphous" fit, and this refinement cycle was then repeated. This gave a satisfactory fit to the acquired diffraction pattern of the sample within the entire Q-range 1 to 3^{-1} Å. This decomposition scheme was applied to the diffraction pattern acquired at each η to find the crystallinity from

$$X_{c-\text{WAXS}} = \sum_\eta I'_{(110)} + I'_{(200)} + I'_{(020)} \Big/ \sum_\eta I'_{total} \qquad (3)$$
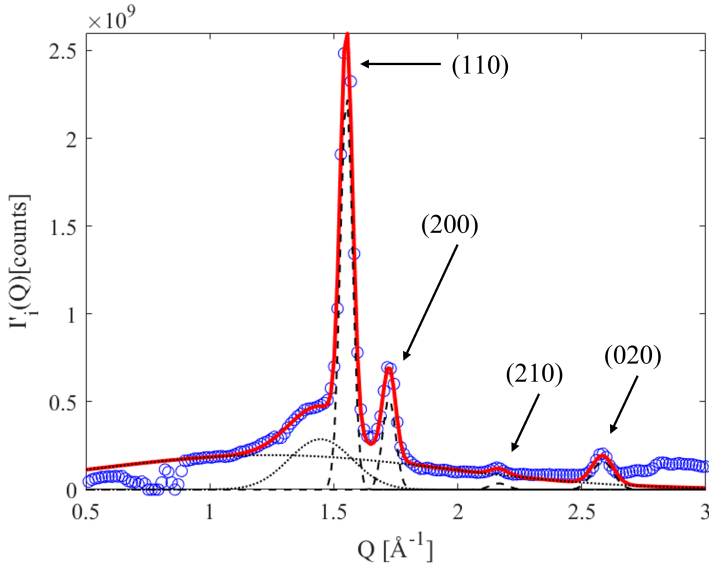
Fig. 4 Model of the diffraction pattern for the unstrained state in the Q-range 0.5 Å^{-1} to 3.0 Å^{-1}. The experimental data (circles) is fitted to the sum of six Gaussian functions (solid line). Four Gaussians represent the four peaks associated with the "crystalline" phase (dashed lines, indexed as peaks in Fig. 3). Two Gaussians (dotted lines) are used for fitting the "amorphous" phase and background.

We compared the fits at each external load step to determine the shifts in positions of the elements. The resulting shifts as function of η were subsequently used to determine the three strain components for each element, cf. Eq. 2. The shifts were found by cross-correlating the strained element with the corresponding unstrained element. The data points for both the strained and unstrained distributions were fitted with a smoothed spline intersecting all identified data points. The resulting intensity distributions for the strained state were cross-correlated with the unstrained reference measurement as illustrated in Fig. 5.

The well defined maximum of the cross-correlation curve is seen to correspond to the maximum position in the strained fit. We estimate the accuracy of this shift in position to be better than twice the distance between interpolation point, 5×10^{-6} Å^{-1}.

4 Results

4.1 Radiation damage test

As a representative result of the beam damage test, the time evolution of the most intense peak, (110), is shown in Fig. 6. For radiation exposures substantially exceeding that of the strain experiment, presented below, we saw no correlated evolution of the position nor the amplitude of the diffraction peaks.
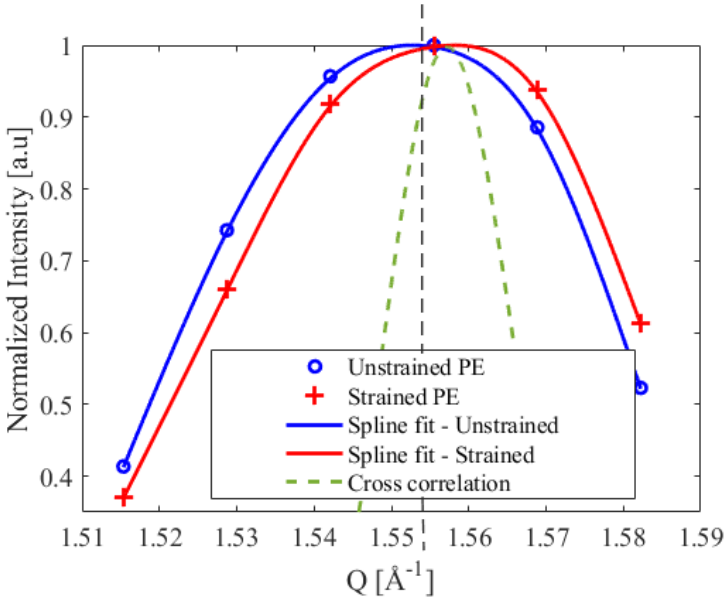
Fig. 5 Illustration of the cross correlation method. Experimental data for the (110) peak for unstrained (circles) and strained (crosses) PE are fitted with splines (blue and red line, respectively). The cross correlation between the two fits is calculated for different shift of the strained curve relative to the origin. The result is overlaid on the plot as a dashed curve. The dashed vertical line is a guide to the eye representing the maximum of the unstrained curve.

The measurement gives us a standard deviation of 2×10^{-4} for relative shift in position and 2×10^{-3} for relative intensity variation. We consider these numbers as an upper limit on the measurement uncertainties of the experiment. Note that the strain sensitivity may be improved by fits to the entire data set. Moreover, as the intrinsic accuracy of the cross correlation methods is more than an order of magnitude better, we conclude that the prime limitation on strain sensitivity in this experiment is signal-to-noise.

In the work by Coffey *et al.* [24] the ratio of crystalline mass for PE is shown to decrease in ionising radiation, whereby the peaks in the diffraction pattern shift position and decrease in amplitude. Coffey *et al.* subjected 100 nm foils of PE to radiation in an inert atmosphere with negligible changes, but in atmospheric oxygen a significant mass conversion was catalysed. Our samples were radiated in atmospheric conditions but the sample thickness was ≈ 2 mm and even with the high oxygen permeability of PE the conversion process may thus on average have been oxygen starved.

4.2 Initial texture

The as-received material was machined into a dogbone. This treatment will not influence the texture of the material except within a surface layer thin enough to not influence the diffraction signal from the bulk. The initial anisotropy is thus originating from the production process. In Fig. 7 the initial anisotropy
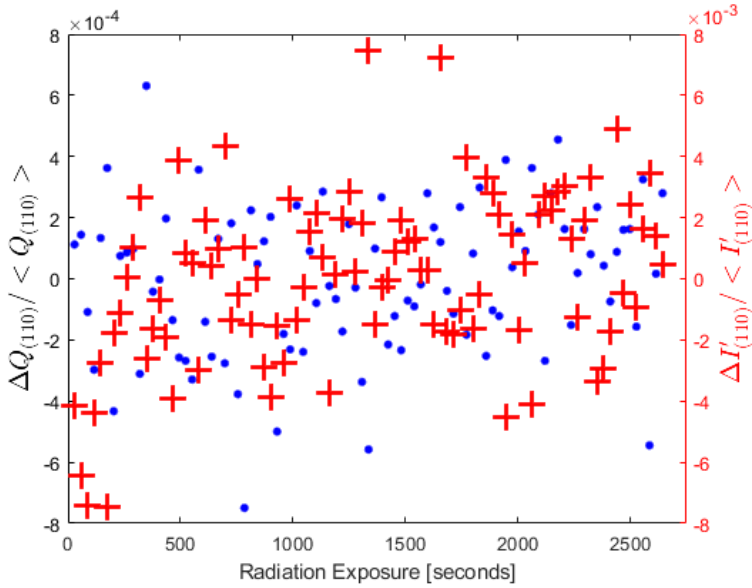
Fig. 6 Radiation damage test. Evolution of properties of the most intense diffraction peak, the (110) peak at $Q = 1.55$ Å^{-1}, as function of exposure time. Each data point represents the median of the results from 12 consecutive diffraction patterns acquired in the span of ≈ 22 seconds exposure including dead time. Blue dots correspond to the position of the peak relative to the average position. The standard deviation is 2×10^{-4}. The red crosses represent the relative amplitude of the peak. The standard deviation is 2×10^{-3}.

of the crystalline peaks are shown. The anisotropic part of the intensity I_A and the average baseline intensity I_{bl} are determined from a fit $I_{\eta,\epsilon_0} = I_{bl} + I_A \sin(\eta + \eta_0)$. The relative amplitude I_A/I_{bl} of this anisotropic part is shown in Fig. 7. The (020) peak exhibit the stronger anisotropy being twice that of the others. Not shown in the figure is the orientation of the initial texture. The initial orientations of (200) is orthogonal to the other peaks and (200) is aligned with the strain direction.

4.3 Strain evolution during tensile deformation

Initially we report on the evolution of strain within the crystalline phases. As an example, the resulting azimuthal variation in position of the (020) peak is shown in Fig 8 with external strain as parameter. An example of a fit of such curves to the expression in Eq. 2 is shown in Fig. 9. The sinusoidal variation is representative of the behaviour of all four "crystalline" peaks at all external loads. (In both Figs. 8 and 9 data points in the azimuthal range from 115° to 155° are excluded, as the beam stop shadows the detector in this range [1]).

The fit of the strain model to the data shown in Fig. 9 is seen as satisfactory. In the remainder of the paper we shall adopt the terminology of $\epsilon_\parallel$ for the axial strain, parallel to the direction of the applied strain, $\epsilon_\perp$ for the tangential

---

[1] For future reference, a beam-stop optimised for the size of the incident beam would be beneficial
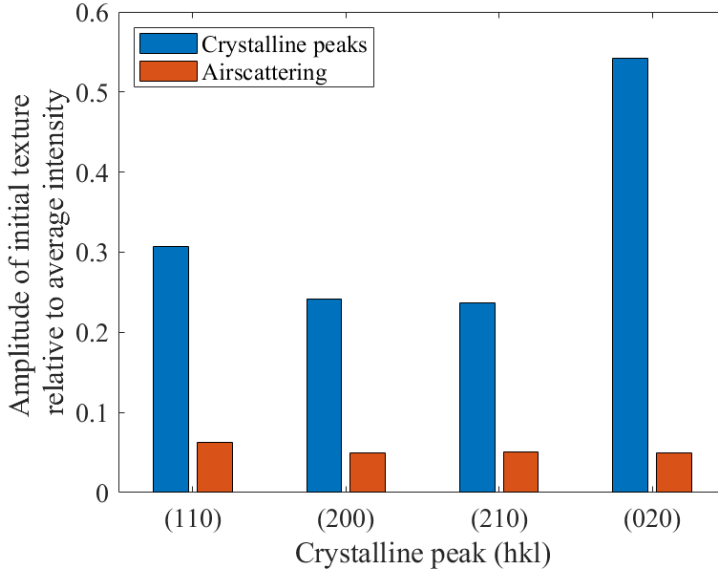
Fig. 7 The initial texture of the four crystalline peaks (blue bars). The azimuthal variation in intensity was fitted with a sine function. Shown is the amplitude of the sine function relative to the median intensity of the peak. To account for variations in detector efficiency and beam polarity the anisotropy - calculated in the same way - is also shown for the corresponding air diffraction signal (red bars).

strain in the perpendicular direction to the applied strain and ϵ_τ for the shear strain.

We note that the residuals, shown in Fig. 9 indicate the possible existence of an additional component to the diffraction model. We expect that a better correction of detector linearity would reduce this residual correlation. Furthermore since the beam width was only slightly smaller than the sample the assumption of an isotropic decrease in intensity for all η could be challenged for higher Q values.

The evolution of the resulting axial ($\epsilon_\parallel$), transverse ($\epsilon_\perp$) and shear (ϵ_τ) strains, are shown in Fig. 10 for the "crystalline" peaks. We call these mesoscopic strains as they are probed on a length scale of nanometers. We note that all components have the sign corresponding to a tensile strain. The mesoscopic and macroscopic strain are close to linearly correlated within the elastic strain range studied and it is therefore reasonable to fit a slope to each of these curves. From this we can determine the ratio $\epsilon_{meso}/\epsilon_{macro}$, where ϵ_{macro} is the macroscopic strain. We also determine the ratio $\epsilon_\perp/\epsilon_\parallel$ between mesoscopic strain perpendicular and parallel to the tensile direction. (Note that we in this experiment only had access to the perpendicular strain along the width dimension of the tensile sample – both for the mesoscopic and macroscopic measurements.)
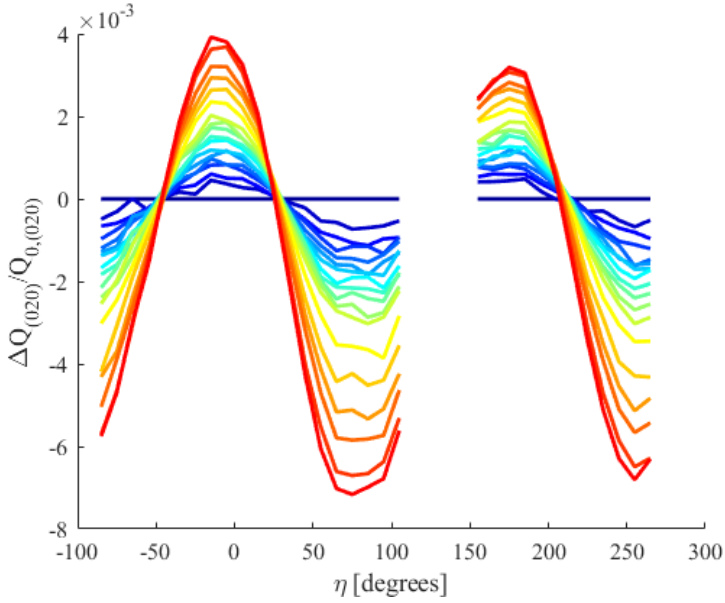
Fig. 8 Analysis of mesoscopic strain. The relative shifts in peak position of the (020) peak are shown as function of the azimuthal angle η. The curves represent increasing external strain (blue through red). Data in the η-range between $115°$ and $165°$ was removed due to interference of the beam-stop with the diffraction signal.
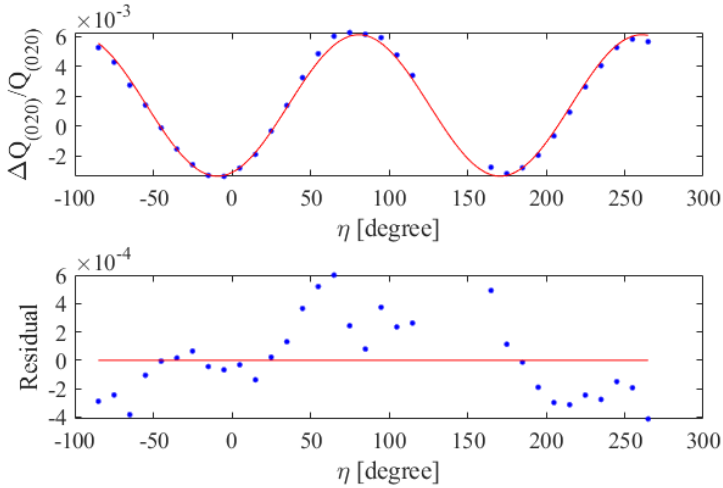

Fig. 9 Above: relative shift in Q of (020) as a function of azimuthal angle η for a global external strain of 6.2% (blue dots). The solid red line is a fit to the function in Eq. 2. Below: the residual when subtracting the fitted values from the experimental data.
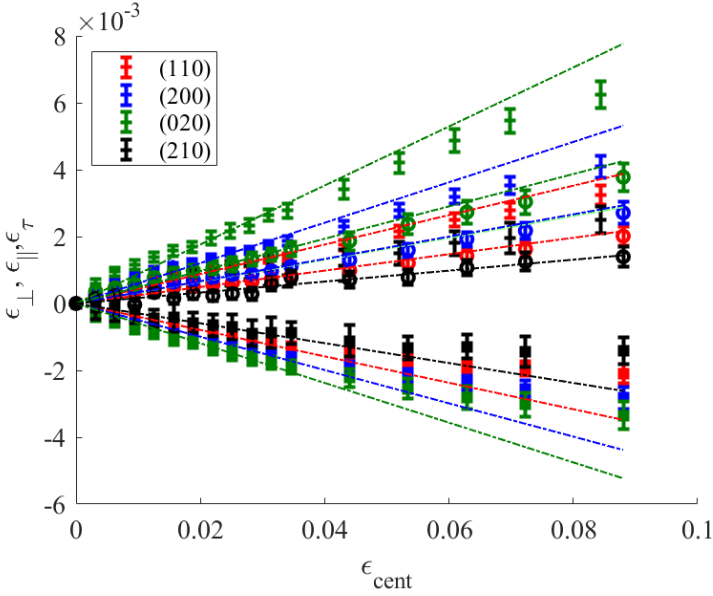
Fig. 10 Mesoscopic strain components for the "crystalline" phases as a function of external strain. The strain components $\epsilon_\perp$ (negative gradients and + markers), and $\epsilon_\parallel$ (positive gradient and + markers) and shear ϵ_τ (o markers) are shown with error bars corresponding to the RMS error of a fit to Eq. 2. The dashed lines represent fits of straight lines through $(0, 0)$ to the data up to a strain of 3%.

Table 1 Table of mesoscopic mechanical parameters resulting from the linear fits in Fig. 10. The macroscopic value for the perpendicular strain are extracted from the optical camera. The macroscopic value for elongation has been adjusted according to the FE calculation in section 2.

	Q Å^{-1}	d Å	$\frac{\epsilon_{macro}}{\epsilon_{cent}}$	$\epsilon_\perp/\epsilon_\parallel$
Macroscopic				0.54 ± 0.1
(110)	1.46-1.63	4.1	30.4 ± 2.1	0.74 ± 0.06
(200)	1.64-1.82	3.6	22.2 ± 1.7	0.73 ± 0.06
(210)	2.1-2.2	3.0	41.9 ± 3.4	0.72 ± 0.06
(020)	2.48-2.68	2.4	15.2 ± 1.0	0.55 ± 0.04

In Table 1 the resulting mesoscopic mechanical parameters are listed. The uncertainties represent the 95% confidence intervals of the gradients in Fig. 10. For the confidence interval each data point is weighed inversely proportional to the errorbars in the same plot.

In this elastic regime the relation between mesoscopic and macroscopic strain are for all peaks a factor between 10 to 40 in correspondence with the notion that the elongation primarily give rise to entropic reconfiguration. Moreover, the ratio decreases continuously with increasing Q (and therefore with decreasing direct space distance r). In fact an inverse relationship:

$\epsilon_{meso}/\epsilon_{macro} \propto 1/Q$ describe the results well except for the peak (210). On the other hand the response of the peaks show no obvious correlation to crystallography. This in contrast to the classical strain response of crystalline materials where bond strength depends on crystallography (Schmidt factors).

From the FE calculation the ratio between strain perpendicular and along the drawing direction from geometric constraint should be 0.34 rather than the traditional macroscopic value found from the Poisson ratio , $\nu = 0.46$ [30]. Both values assumes an isotropic material and even with fairly high uncertainty on these numbers the results indicate this is not the case. To resolve this question, information from the depth dimension of our test specimen is required.

We conclude that the mesoscopic mechanical response of the "crystalline" phases is very different from that of a classical crystalline material due to the dominant role of the softer amorphous phase. When the material is elongated, part of the energy is absorbed in entropic reconfigurations of the polymers. This leads to different shells in the atomic pair correlation function responding differently, similar to the response of glasses [11]. It is however, intriguing that (within the crystalline phase) the shells become harder with increasing average distance r, while in the macroscopic limit, the response is soft. This is in direct contrast to the response of glasses.

4.4 Texture evolution during tensile deformation

It is relevant to compare the strain evolution at different length scales to the reorientation taking place at the same scales. To describe the evolution in orientation distribution we determine the intensity of each of the four tracked elements in the model for each of the segments defined in Eq. 1. Specifically, the intensity distribution of an element is integrated over the Q-range defined in Table 1. In Fig. 11 the variation with η is shown for each of the "crystalline" peaks at the maximum external strain.

A sinusoidal behavior is observed for all peaks corresponding to a change in intensity along and perpendicular to the external strain direction. The intensity for peaks (110), (200) and (210) increase for η perpendicular to the strain direction. The opposite is true for (020) where a (smaller) increase is observed for the parallel direction. The four peaks related to the orthorhombic phase all lie in the (hk0) plane and are consistent wrt. texture.

For each external strain level, curves similar to Fig. 11 are fitted to a sine function

$$I_{\eta,\epsilon}/I_{\eta,\epsilon_0} = I_{bl} + I_A \sin(\eta + \eta_0) \tag{4}$$

We use the ratio of the amplitude to the baseline I_A/I_{bl} as a measure of the texture evolution. The resulting texture evolution is presented in Fig. 12, for direct comparison with Fig. 10. The overall correlation between orientation change and external load is seen as a manifestation of increased chain alignment in the "crystalline" phases. For peaks (110) and (200) we note that the
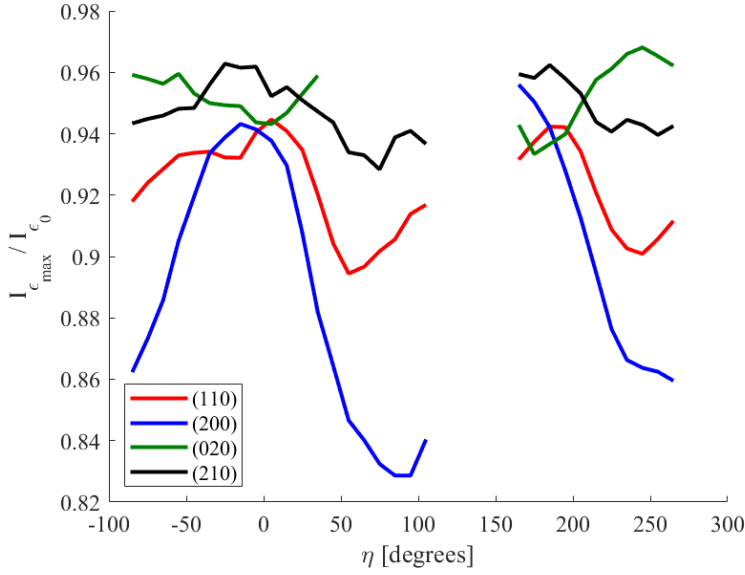
Fig. 11 Texture for the maximal external load. The relative intensity difference between fully strained and unstrained state for the 4 crystalline peaks is shown. The mean relative intensity is lower for all peaks due to a decrease in sample thickness.
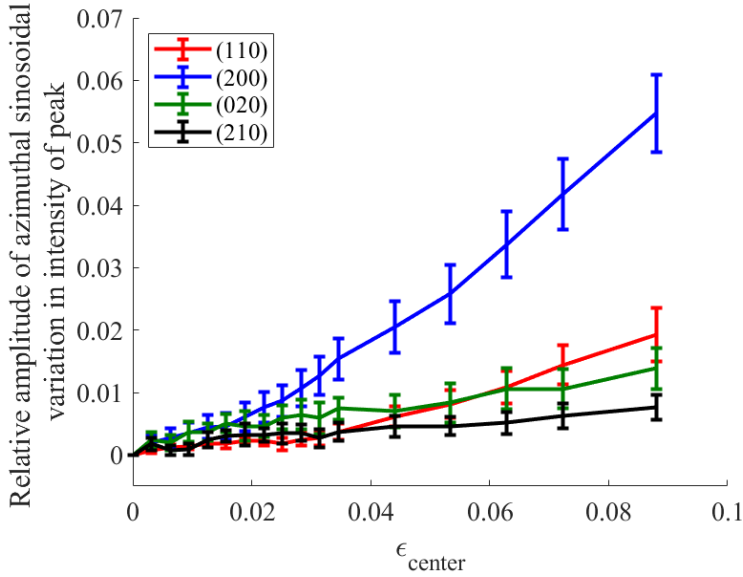

Fig. 12 Texture evolution. The relative amplitude of the sinosoidal variation of the intensity difference compared to zero external strain as a function of the external strain. This parameter corresponds to the shift in texture from the initial value as the polymer chains align in the direction of external strain. Errorbars represents the RMS error of a fit to Eq. 4.
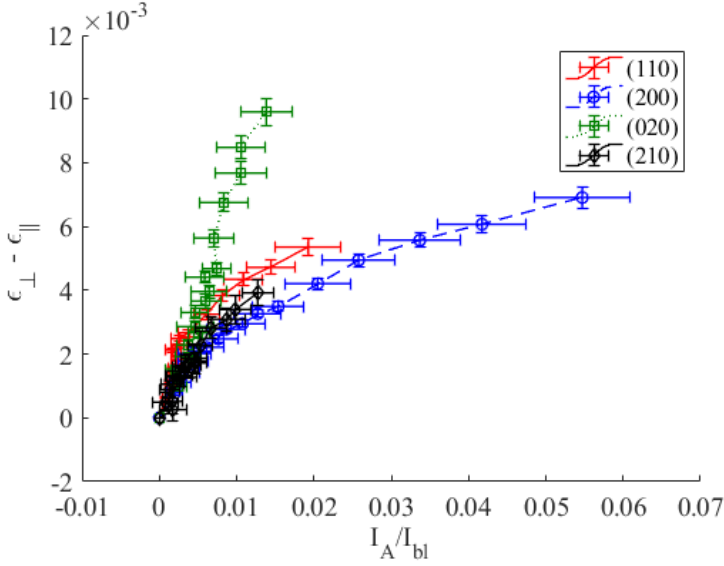
Fig. 13 Correlation of mesoscopic strain ϵ and texture for peaks 1 to 4. The difference between strain components, $\epsilon_\perp - \epsilon_\parallel$, and the anisotropy $I_A/I_b l$ is shown.

development of texture increases with Q, and therefore is inversely related to r. Hence, the innermost bonds appear to have more degrees of freedom to rotate. This surprising result mimics that of the strain variation with Q, see Table 1.

In the previous work on mesoscale strain in elastomers, a linear correlation was reported between the difference between the inter-chain strain components, and the inter-chain ordering – measured by the relative intensity difference of the first sharp diffraction peak at $(\eta = 0°)$ and $(\eta = 90°)$ [23] This is the anisotropy I_A/I_{bl}. The corresponding plot for the four "crystalline" peaks of PE is shown in Fig. 13. Evidently, there is no universal curve and at least three of the curves are clearly non-linear.

4.5 Crystallinity

The PE sample was measured with differential scanning calorimetry (DSC) to 50.1 % in the as-recieved state. In the Q-range of 0.5 to 2.5 Å we assess the integrated intensity of the diffraction signal for the crystalline and the amorphous phases respectively based on the decomposition model illustrated in Fig. 4. Determined in this way, initially the crystalline phase comprise 50.5 % of the total material.

The evolution of this x-ray measured crystallinity ratio with the external load is shown in Fig. 14. As expected [31] the crystalline fraction are constant up to the end of the linear regime and afterwards decreases very slightly with load and at a rate that is much lower than the corresponding evolution in texture.
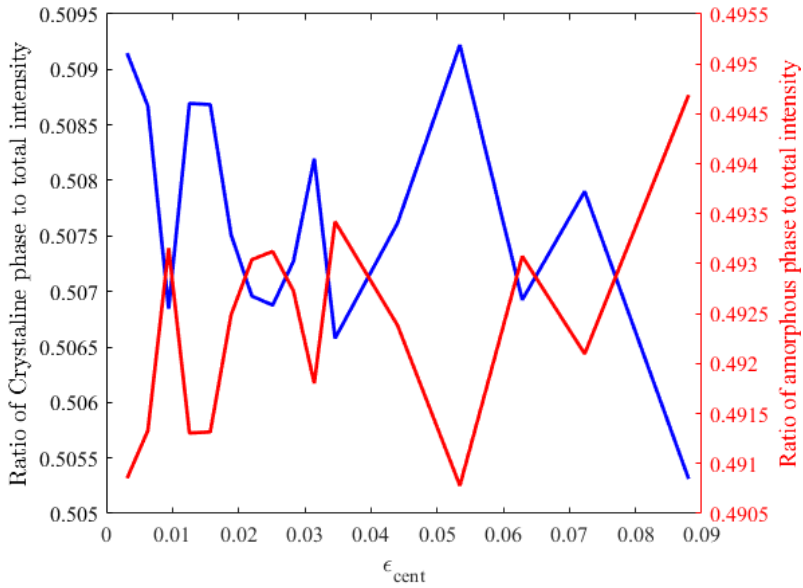
Fig. 14 Evolution in crystallinity with external strain. Shown in blue is the ratio of the integrated intensity associated with the crystalline phases and the total integrated intensity. Shown in red is the corresponding curve for the amorphous phase. The crystalline phase intensity is determined as the total integrated intensity of the Gaussian peak fits from the decomposition.

4.6 Data analysis approach

The method presented offers a unique possibility for testing micro-mechanical models of the response of thermoplasts like PE on several length scales. However, for basic research we would recommend to use an atomic model to interpret the diffraction data and an improved data analysis pipeline, similar to the previous work on mesoscale strain in inorganic glasses [11] and elastomers [23]. Deriving direct space correlation functions and performing a PDF analysis of the data is relevant, and would give direct information on the evolution of interatomic bond-length as well as a better separation of the two phases. Knowing the molecular structure of the two phases one can also provide more detailed and accurate models that predict the diffracted intensity pattern. Likewise Legendre polynomials provide a better description of the texture evolution [23].

For use in engineering, however, the present data analysis approach is well suited: the analysis of shifts of peaks in Q-space does not require any *a priori* knowledge of the molecular structure nor advanced data analysis tools (beyond cross correlation). Hence, it seems likely that it can find application also for less ideal instrumental settings and for unknown materials.

4.7 Applicability of the mesoscale strains as a tool in engineering

A motivation for this work is the perspective of using the mesoscale strains as a local strain gauge for inspection and for interfacing with mechanical modelling. The fact that within the external strain range studied, the response is linear on all length scales, and for both phases implies that we can assume that any of these probes is proportional to the "relevant" length scale for e.g. the initiation of failure. For PE it would therefore be natural to focus on the shift of the most intense peak. It is also noteworthy that the texture evolution is not linear, and hence a less likely candidate as a proxy for determining the local macroscopic strain.

The accuracy of the mesoscopic strain determination was determined to be 5×10^{-6} in the absence of signal-to-noise issues. Moreover, the uncertainty on strain arising from a single segment was determined in section 4.1 to be 2×10^{-4}. There is strong evidence from strain characterisation of other materials that this error will be "quenched" when performing the joint fit to all segments, by an amount of approximately $\sqrt{36}$. From this we make the tentative conclusion that a sensitivity of mesoscopic strains of order 3×10^{-5} is within reach. Using the correlation between mesoscopic and macroscopic strain provided in table 1, the sensitivity to local macroscopic strain becomes below 10^{-3}. This is an excellent result, that however eventually need verification by definition and use of strain scanning standards.

As an input to a mechanical model the results presented may be insufficient as the strain of the amorphous component is absent and not all components were probed for the crystalline phase. We did perform a similar analysis to that presented in sections 4.2-4.4 for the amorphous component, and found indications of a load sharing. However, issues with the beamstop (and also a too primitive model of $S(Q)$ for this phase) implied that the uncertainties on the results are too high. We are confident though, that the strain evolution of the amorphous phase can be found from optimised experiments.

The generalisation to provision of all strain components is straight forward and only requires repeating the study at 2 or more projections. The relevant rotation is readily available at any instrument that support diffraction or (diffraction) tomography.

4.8 Outlook

Similar to previous work on crystals and glasses, the next step is to extend the characterisation to mapping of 2D or 3D strain fields by scanning slits [32], wires [9], micro-channel plates [33] or coded apertures through the diffracted signal. Such 3D maps would in a unique way facilitate comparison with 3D micro-mechanical modelling, for guidance and validation of the models.

The prospect of application are wide ranging and includes studies of composite materials to understand structural integrity and degradation, materials

for high voltage applications to identify regions with decreased insulation capabilities and soft robotics utilised in e.g prosthetics. Stress and strain fields are hard to identify inside complex structures using conventional measurement techniques and the challenges cover many length scales. Medico products based on polymers often rely on build-in stresses in its application. Contrary to this and at a larger scale, adhesive joints of cm thicknesses in wind turbine blades can develop local damage due to build in stresses [34].

5 Conclusion

We have presented a simple analysis scheme to extract local strain components with high accuracy from semicrystaline polymers. In the elastic strain regime of PE we have shown that the correlation between average strain and local mesoscopic strain is linear at all length scales.

The method simultaneously extracts the evolution of texture. For PE the texture exhibited a nonlinear response to the externally applied strain making it less suitable as a proxy for describing the local strain in engineering applications.

This work also makes it clear that the mesoscopic response to the stress field is very dependent on length scale. For polyethylene the response for (020) was 2.1 times higher than the otherwise most prominent component the (110) peak. To obtain quantitative measurements of the local macroscopic strain field from this method for a certain (class of) materials it is thus necessary to have performed a calibration experiment to understand the mesoscopic response and to identify the most sensitive component.

Declarations

- Conflict of interest The authors have no conflicts of interest to declare that are relevant to the content of this article.
- Ethics approval Not applicable
- Consent to participate Not applicable
- Consent for publication Not applicable
- Availability of data and materials Data is avaiable upon request
- Code availability Code is not available at this time
- Authors' contributions Not applicable

References

[1] Noyan, I.C., Cohen, J.B.: Residual Stress. Springer, Berlin (1987)

[2] Fitzpatrick, M., Lodini, A.: Analysis of Residual Stress by Diffraction Using Neutron and Synchrotron Radiation. Taylor and Francis, London (2003)

[3] Kirkpatrick, P., Baez, A.V., A., N.: Geometrical optics of grazing incidence reflectors. Phys Rev. **73**, 535–536 (1948)

[4] Snigirev, A., Kohn, V.G., Snigireva, I.I., Lengeler, B.: A compound refractive lens for focusing high-energy x-rays. Nature **384**, 49 (1996). https://doi.org/10.1038/384049a0

[5] Pfeiffer, F., David, C., Burghammer, M., Riekel, C., T., S.: Two-dimensional x-ray waveguides and point sources. Science **297**, 230–234 (2002). https://doi.org/10.1126/science.1071994

[6] Morgan, A.J., Prasciolu, M., Andrejczuk, A., Krzywinski, J., Meents, A., Pennicard, D., Graafsma, H., Barty, A., Bean, R.J., Barthelmess, M., Oberthuer, D., Yefanov, O., Aquila, A., Chapman, H.N., Bajt, S.: High numerical aperture multilayer laue lenses. Sci. Rep. **5**, 9892 (2015). https://doi.org/10.1038/srep09892

[7] Reimers, W., Pyzalla, A., Broda, M., Brusch, G., Dantz, D., Schmackers, T., Liss, K., Tschentscher, T.: The use of high-energy synchrotron diffraction for residual stress analyses. J. Mater. Sci. Lett. **18**, 581–583 (1999)

[8] Poulsen, H.F., Nielsen, S.F., Lauridsen, E.M., Schmidt, S., Suter, R., Lienert, U., Margulies, L., Lorentzen, T., Juul Jensen, D.: Three-dimensional maps of grain boundaries and the stress state of individual grains in polycrystals and powders. Journal of applied crystallography **34**(6), 751–756 (2001). https://doi.org/10.1107/S0021889801014273

[9] Larson, B.C., Yang, W., Ice, G.E., Budai, J.D., Tischler, J.Z.: Three-dimensional x-ray structural microscopy with submicrometre resolution. Nature **415**, 887–890 (2002). https://doi.org/10.1038/415887a

[10] Simons, H., King, A., Ludwig, W., Detlefs, C., Pantleon, W., Schmidt, S., Stöhr, F., Snigireva, I., Snigirev, A., Poulsen, H.F.: Dark field x-ray microscopy for multiscale structural characterization. Nat. Commun. **6**, 6098 (2015). https://doi.org/10.1038/ncomms7098

[11] Poulsen, H.F., Wert, J.A., Neuefeind, J., Honkimäki, V., Daymond, M.: Measuring strain distributions in amorphous materials. Nature Mater. **4**,

33–36 (2005). https://doi.org/10.1038/nmat1266

[12] Lunt, A.J.G., Chater, P., Korsunsky, A.M.: On the origins of strain inhomogeneity in amorphous materials. Sci. Reports **8**, 1574 (2018). https://doi.org/10.1038/s41598-018-19900-2

[13] Guevara-Morales, A., Figueroa-López, U.: Residual stresses in injection molded products. Journal of Materials Science **49**(13), 4399–4415 (2014). https://doi.org/10.1007/s10853-014-8170-y

[14] Pepin, J., Gaucher, V., Rochas, C., Lefebvre, J.M.: In-situ SAXS/WAXS investigations of the mechanically-induced phase transitions in semi-crystalline polyamides. Polymer **175**, 87–98 (2019). https://doi.org/10.1016/J.POLYMER.2019.04.073

[15] Xiong, B., Lame, O., Chenal, J.M., Rochas, C., Seguela, R., Vigier, G.: In-situ SAXS study of the mesoscale deformation of polyethylene in the pre-yield strain domain: Influence of microstructure and temperature. Polymer **55**(5), 1223–1227 (2014). https://doi.org/10.1016/J.POLYMER.2014.02.004

[16] Humbert, S., Lame, O., Chenal, J.M., Rochas, C., Vigier, G.: Small strain behavior of polyethylene: In situ SAXS measurements. Journal of Polymer Science Part B: Polymer Physics **48**(13), 1535–1542 (2010). https://doi.org/10.1002/POLB.22024

[17] Millot, C., Séguéla, R., Lame, O., Fillot, L.A., Rochas, C., Sotta, P.: Tensile Deformation of Bulk Polyamide 6 in the Preyield Strain Range. Micro-Macro Strain Relationships via in Situ SAXS and WAXS. Macromolecules **50**(4), 1541–1553 (2017). https://doi.org/10.1021/acs.macromol.6b02471

[18] Asp, L.E., Berglund, L.a., Talreja, R.: A criterion for crack initiation in glassy polymers subjected to a composite-like stress state. Composites Science and Technology **56**(11), 1291–1301 (1996). https://doi.org/10.1016/S0266-3538(96)00090-5

[19] Zobeiry, N., Forghani, A., Li, C., Gordnian, K., Thorpe, R., Vaziri, R., Fernlund, G., Poursartip, A.: Multiscale characterization and representation of composite materials during processing. Philosophical Transactions of the Royal Society A: Mathematical, Physical and Engineering Sciences **374**(2071) (2016). https://doi.org/10.1098/rsta.2015.0278

[20] Nishida, M., Kitamura, M., Hanabusa, T., Matsue, T.: X-ray Residual Stress Measurement of Fiber Reinforced Plastic Composite. Journal of Solid Mechanics and Materials Engineering **4**(8), 1178–1185 (2010). https://doi.org/10.1299/jmmp.4.1178

[21] Hughes, D.J., Heeley, E.L., Curfs, C.: A non-destructive method for the measurement of residual strains in semi-crystalline polymer components. Materials Letters **65**(3), 530–533 (2011). https://doi.org/10.1016/j.matlet.2010.10.046

[22] Schneider, K.: Investigation of structural changes in semi-crystalline polymers during deformation by synchrotron X-ray scattering. Journal of Polymer Science Part B: Polymer Physics **48**(14), 1574–1586 (2010). https://doi.org/10.1002/polb.21971

[23] Neuefeind, J., Skov, A.L., Daniels, J.E., Honkimäki, V., Jakobsen, B., Oddershede, J., Poulsen, H.F.: A multiple length scale description of the mechanism of elastomer stretching. RSC Adv. **6**, 95910 (2016). https://doi.org/10.1039/C6RA22802J

[24] Coffey, T., Urquhart, S.G., Ade, H.: Characterization of the effects of soft X-ray irradiation on polymers. Journal of Electron Spectroscopy and Related Phenomena **122**(1), 65–78 (2002). https://doi.org/10.1016/S0368-2048(01)00342-5

[25] Howard, S.: Materials Data Book. Cambridge University Engineering Department, Cambridge, UK (2003)

[26] Van Driel, T.B., Kjær, K.S., Hartsock, R.W., Dohn, A.O., Harlang, T., Chollet, M., Christensen, M., Gawelda, W., Henriksen, N.E., Kim, J.G., *et al.*: Atomistic characterization of the active-site solvation dynamics of a model photocatalyst. Nature communications **7**(1), 1–7 (2016). https://doi.org/10.1038/ncomms13678

[27] Bunn, C.W.: The crystal structure of long-chain normal paraffin hydrocarbons. The "shape" of the CH2 group. Transactions of the Faraday Society **35**, 482–491 (1939)

[28] Rice, J.R.: Solid Mechanics. Harvard University, Boston (2010)

[29] Monar, K., Habenschuss, A.: Modeling the principal amorphous halo in quiescent melts of polyethylene and ethylene copolymers using wide-angle X-ray scattering and its implications. Journal of Polymer Science Part B: Polymer Physics **37**(24), 3401–3410 (1999). https://doi.org/10.1002/(SICI)1099-0488(19991215)37:24$\langle$3401::AID-POLB3/$\rangle$\$3.0.CO;2-Y

[30] CROW: Chemical Retrieval on the Web (CROW) - Polymer Properties Database. Accessed = 2020-07-02 (2020). https://polymerdatabase.com/polymerphysics/PoissonTable.html

[31] Chang, B., Schneider, K., Xiang, F., Vogel, R., Roth, S., Heinrich, G.: Critical Strains for Lamellae Deformation and Cavitation during Uniaxial

Stretching of Annealed Isotactic Polypropylene. Macromolecules **51**(16), 6276–6290 (2018)

[32] Lienert, U., Martins, R., Grigull, S., Pinkerton, M., Poulsen, H.F., Kvick, Å.: High spatial resolution strain measurements within bulk materials by slit-imaging. Mater. Res. Soc. Symp. Proc. **590**, 241–246 (2000). https://doi.org/10.1557/PROC-590-241

[33] Wroblewski, T., Breuer, D., Crostack, H., Fandrich, F., Gross, M., Klimanek, P.: Mapping in real and reciprocal space. Mater. Sci. Forum **278-281**, 216–220 (1998). https://doi.org/10.4028/www.scientific.net/MSF.278-281.216

[34] Jørgensen, J.B., Sørensen, B.F., Kildegaard, C.: Tunneling cracks in full scale wind turbine blade joints. Engineering Fracture Mechanics **189**, 361–376 (2018). https://doi.org/10.1016/j.engfracmech.2017.11.016